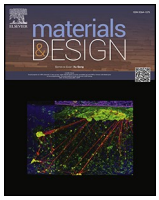
Materials & Design 268 (2026) 116430



Contents lists available at ScienceDirect

Materials & Design

journal homepage: www.elsevier.com/locate/matdes



Thermoelastic optimisation of fibre-steered composite mirrors for space-based laser communication systems

Nenglong Yang [a,*], Georgios Stamatopoulos [b], Sampreet Sabarad [a], Alex Skordos [a], Geoffrey Neale [a]

[a] Centre for Materials, Faculty of Engineering and Applied Science, Cranfield University, MK43 0AL, UK
[b] iCOMAT Ltd., Bristol BS3 2UN, UK

ARTICLE INFO

Keywords:
A. Polymer-matrix composites (PMCs)
B. Thermomechanical
C. Finite element analysis (FEA)
C. Process modelling

ABSTRACT

Lightweight, dimensionally stable mirrors are essential for space-based laser communication, requiring concurrent optimisation of mass, stiffness, and environmental stability. This study presents a novel design–manufacture–validation framework that explicitly links variable-stiffness laminate design, manufacturing-induced effects, and experimentally validated optical performance under identical conditions. The novelty lies in providing the first experimentally validated, like-for-like comparison between conventional straight-fibre and Rapid Tow Shearing (RTS) laminates for precision composite mirrors under identical geometry, loading conditions, manufacturing assumptions, and validation procedures. The framework combines finite-element structural, thermoelastic, and hygroscopic analyses with Cure Hardening Instantaneously Linear Elastic (CHILE)-based process modelling and demonstrator-level validation for a 0.50 m composite mirror. Both designs satisfy the $>$ 140 Hz fundamental frequency requirement and exhibit large safety margins. The straight-fibre laminate achieves $\sim$ 153 Hz and $\sim$ 69 μm RMS, while the RTS laminate achieves $\sim$ 145 Hz with comparable deformation and $\sim$ 11% lower mass. Hygroscopic effects are modest, and cure-induced distortion is dominated by low-order modes. The results demonstrate that RTS enables mass-efficient stiffness tailoring without degrading first-order thermoelastic performance and establish a validated methodology linking modelling predictions, manufacturing variability, and measured surface figure for next-generation lightweight space optics.

1. Introduction

Lightweight, thermally stable mirrors are critical for space optical systems, including telescopes and laser communication payloads. As aperture and pointing requirements increase, conventional materials such as glass and beryllium provide excellent optical quality but impose mass penalties that scale unfavourably with size [1]. Carbon fibre–reinforced polymer (CFRP) laminates offer an attractive alternative due to their high specific stiffness, low areal density, and tailorable coefficients of thermal expansion (CTE) [2]. These attributes are particularly important in low Earth orbit (LEO), where thermal cycling, support constraints, and moisture desorption drive out-of-plane deformation and optical wavefront error (WFE).

Beyond conventional straight-ply laminates, additional structural efficiency can be achieved using variable-stiffness designs, in which fibre orientations vary spatially to tailor stiffness distribution and deformation response [3,4]. Early approaches such as Tailored Fibre Placement (TFP) are limited in scalability, while Automated Fibre Placement (AFP) can introduce defects (e.g., wrinkling, bridging, tow gaps) when steering relatively wide tows along tight curvatures, typically at steering radii on the order of a few hundred millimetres or below [5]. Continuous Tow Shearing (CTS) and, more recently, Rapid Tow Shearing (RTS) address these limitations by steering via controlled in-plane shear, enabling smooth orientation changes with reduced defect propensity. Additionally, RTS introduces shear–thickness coupling, providing a mechanism to tailor both stiffness and thickness simultaneously [3,6]. Consequently, RTS enables spatially varying stiffness with improved manufacturability using aerospace-grade prepregs [7,8]. However, shear-induced thickness variation and fibre distortion can introduce local non-uniformities and increase process sensitivity, particularly at high shear angles [3].

Despite their demonstrated capabilities in structural applications, particularly with respect to buckling and vibration tailoring [9–11], the application of variable stiffness laminates to precision mirrors remains

* Corresponding author.
E-mail address: Nenglong.Yang@cranfield.ac.uk (N. Yang).

https://doi.org/10.1016/j.matdes.2026.116430
Received 19 May 2026; Received in revised form 15 June 2026; Accepted 16 June 2026
Available online 17 June 2026
0264-1275/© 2026 The Authors. Published by Elsevier Ltd. This is an open access article under the CC BY license (http://creativecommons.org/licenses/by/4.0/).

unexplored. Optical performance is governed by thermoelastic, hygroscopic, and process-induced deformation rather than ultimate strength. For reflective optics, micrometre-scale surface displacements translate directly into optical path difference and WFE, making dimensional stability the primary design driver. Quantitative, like-for-like assessments of RTS for precision composite mirrors, under consistent geometry, boundary conditions, environmental loading, and manufacturing effects, remain limited [12].

A key limitation in existing studies is the lack of integrated assessment linking laminate design, manufacturing-induced residual stress, and measured surface figure. Process-induced effects such as cure shrinkage, tool–part interaction, and thickness variations are known to significantly influence final part distortion and shape development [13], yet they are often analysed independently of structural optimisation frameworks, despite their strong coupling with laminate behaviour and final geometry. Experimental validation of variable-stiffness composite mirrors, particularly with full-field metrology and thermo-mechanical testing, remains scarce.

To address these gaps, this work introduces a like-for-like design–manufacture–validation framework for CFRP composite mirrors, explicitly linking variable-stiffness laminate design, manufacturing-induced effects, and experimentally measured optical performance under consistent conditions. The framework combines finite-element structural, thermoelastic, and hygroscopic analyses, Cure Hardening Instantaneously Linear Elastic (CHILE)-based process modelling of cure-induced distortion, manufacturing assessment, and comprehensive demonstrator-level validation, including coordinate metrology, Zernike decomposition, thermo-mechanical testing, Differential Scanning Calorimetry (DSC), and flexural testing, to quantify the mass–stability trade-off between straight-fibre and RTS laminates. The framework is integrated by consistently linking these stages within a unified workflow; however, the individual analyses are not embedded within a single automated optimisation loop. The resulting contribution is a validated and transferable methodology for the design of lightweight composite mirrors, together with new insight into the extent to which stiffness tailoring can improve optical performance in space-based laser communication systems. The remainder of the paper summarises relevant prior work and optical stability considerations, describes the modelling and optimisation methodology, presents comparative results for process deformation and structural and environmental loading, and concludes with experimental validation and discussion of the key design drivers for composite mirrors.

2. Composite mirrors for space telescopes and laser communication

2.1. Structural and environmental requirements

Large-aperture space optical systems require mirror substrates that combine low mass with high static and dynamic stiffness, while maintaining dimensional stability across the operational thermal environment. Segmented lightweight architectures, exemplified by the James Webb Space Telescope, demonstrate the system-level benefit of reducing mirror mass without compromising optical performance [14]. CFRP substrates are therefore attractive as they offer high specific stiffness and tailorable in-plane CTE, enabling substantial mass reduction relative to glass and metallic mirrors [15]. Previous studies have reported CFRP mirrors with areal densities of $\sim$ 10–20 kg·m^{-2}, with lower values achievable for reduced-stiffness applications [16,17]. In this work, mass is evaluated at the substrate level to ensure consistent comparison between laminate concepts.

Laser communication payloads typically operate in the near-infrared (e.g., 1.55 μm), where surface-quality requirements are less stringent than diffraction-limited visible imaging. Dimensional stability remains the governing requirement, as surface deformation directly translates into optical path difference (OPD) and WFE [18]. The mirror considered in this work serves as the spherical primary in a Schmidt–Cassegrain configuration and includes a central aperture, which locally reduces bending stiffness and influences global deformation behaviour. Consequently, the design emphasis is on minimising areal density, environmental and process-induced out-of-plane deformation while satisfying launch stiffness and strength constraints.

Mirrors in LEO experience repeated thermal excursions and vacuum exposure. For polymer-matrix composites, these conditions drive thermoelastic distortion, moisture desorption strain, and long-term property evolution [19]. Experimental evidence from the Materials International Space Station Experiment programme indicates that CFRP mirrors can maintain dimensional stability in orbit when designed and produced appropriately [20]. However, deformation is typically dominated by low-order global modes (e.g., focus and astigmatism) arising from laminate anisotropy, support conditions, and residual stresses. These modes are critical because low-order errors may be partially correctable, whereas higher-order distortions directly degrade optical performance. Accordingly, key performance drivers are areal density, first-mode frequency, and thermo-hygro-mechanical stability, with emphasis on controlling low-order deformation and manufacturing-induced residual shape.

2.2. Optical figure stability constraints in LEO

LEO mirrors must preserve surface figure under coupled thermal, mechanical, and environmental loads that exceed typical terrestrial conditions [18]. For this study, a representative sun-synchronous orbit ($\sim$570 km altitude) is assumed, implying frequent thermal cycling over the mission lifetime [21]. Temperature variations generate stress and deformation due to anisotropic laminate expansion and potential mismatch with reflective coatings, motivating low-CTE designs and sufficient in-plane thermal conductivity to limit gradients [22]. Launch survivability imposes an additional constraint where the fundamental frequency must exceed 140 Hz to avoid coupling with launch excitation, directly linking stiffness to laminate architecture and support configuration [23].

Optical performance is governed by WFE rather than absolute surface form. For reflective optics at near-normal incidence, an out-of-plane displacement δ produces OPD $\approx 2\delta$, such that a surface RMS of $\sim$ 10 μm corresponds to $\sim$ 20 μm OPD RMS after removal of piston, tilt, and defocus [24,25]. This places stringent requirements on RMS stability while emphasising the importance of deformation mode content. In this work, optical performance is therefore assessed using the RMS surface error after removal of piston, tilt, and defocus (i.e., best-fit sphere), as this metric represents the residual wavefront error relevant to beam quality in laser communication systems. For optical communication at near-infrared wavelengths ($\sim$1.55 μm), surface errors on the order of tens of micrometres RMS are acceptable due to the longer wavelength and relaxed diffraction requirements compared to imaging systems. Accordingly, the reported RMS values are interpreted as application-relevant indicators of optical performance rather than absolute optical-quality limits.

Low-order errors may be partially compensated at system level, whereas higher-order residuals directly degrade beam quality. Accordingly, this work focuses on substrate-level passive stability, minimising thermal- and moisture-driven deformation while accounting for cure-induced shape change under representative boundary conditions. Uniform temperature fields are used to establish controlled, comparable baselines between laminate concepts, while recognising that in-orbit gradients may introduce additional non-axisymmetric deformation. Secondary effects (e.g., coating ageing and radiation exposure) are acknowledged but excluded from the present scope [26].

3. Methodology

3.1. Structural modelling and dynamic analysis

The mirror substrate was analysed under load cases representative of launch and on-orbit operation, using boundary conditions that approximate the corresponding support configurations. The geometry consists of a 0.50 m diameter spherical dish with radius of curvature $R = 8$ m and a 50 mm central aperture (Fig. 1). For a spherical mirror, the paraxial focal length is $f \approx R/2$, giving a nominal f-number of ~ 8.

Finite-element models were developed in Abaqus/Standard [27] using reduced-integration quadrilateral shell elements (S4R). The laminate, which was made of IM7/8552 carbon/epoxy prepreg [28], was defined about the shell mid-surface, with ply orientations referenced to a global material coordinate system to ensure consistency across the aperture. A structured mesh of approximately 8370 elements (~5 mm nominal size) was selected based on a mesh refinement study; further refinement changed the computed surface RMS displacement by $< 2\%$, indicating sufficient convergence. The laminate was modelled as a continuous stacking sequence over the full aperture, representing an idealised uniform substrate without local reinforcement. Orthotropic elastic properties for the IM7/8552 carbon epoxy system were taken from literature (Table 1) [29,30]. All plies were modelled as linearly elastic orthotropic laminae, as predicted stresses remained well below failure allowables.

Launch support was idealised as an eight-point whiffle-tree, with supports located on two concentric rings at radii $r = 106$ mm and $r = 206$ mm. Each support was implemented by coupling a rear-surface patch to a reference point positioned 50 mm along the local surface normal, distributing reactions to avoid local constraint artefacts. Quasi-static launch loads were applied as uniform body accelerations in the axial and lateral directions. Random vibration was represented using a static-equivalent acceleration derived from the Miles relation, based on the qualification spectrum and computed first-mode frequency [31]. This vibration screening is linked to the application-driven launch survivability requirements, according to which spacecraft structures must withstand broadband dynamic excitation without resonance coupling. A linear perturbation eigenvalue analysis under launch boundary conditions was used to verify that the fundamental frequency exceeded the 140 Hz requirement [23], ensuring consistency between the vibration

Table 1
IM7/8552 lamina properties used in the thermoelastic FE model [29,30].

Parameter	Symbol	Value	Unit
Mechanical Properties			
Longitudinal modulus	E_{11}	162.1	GPa
Transverse moduli	E_{22}/E_{33}	8.96	GPa
Major Poisson's ratio	ν_{12}	0.27	–
In-plane shear moduli	G_{12}/G_{13}	4.69	GPa
Through thickness shear modulus	G_{23}	3.09	GPa
Longitudinal tensile strength	S_{11}^{T}	2211.8	MPa
Longitudinal compressive strength	S_{11}^{C}	1731.5	MPa
Transverse tensile strength	S_{22}^{T}	64.1	MPa
Transverse compressive strength	S_{22}^{C}	285.7	MPa
In-plane shear strength	S_{12}	53.5	MPa
Thermal Properties			
In-plane CTE	α_{11}	-5.5×10^{-6}	K^{-1}
Through thickness CTE	α_{22}/α_{33}	25.8×10^{-6}	K^{-1}
Other Properties			
Density	ρ	1.58	g/cm^3
Cured ply thickness	t	0.131	mm

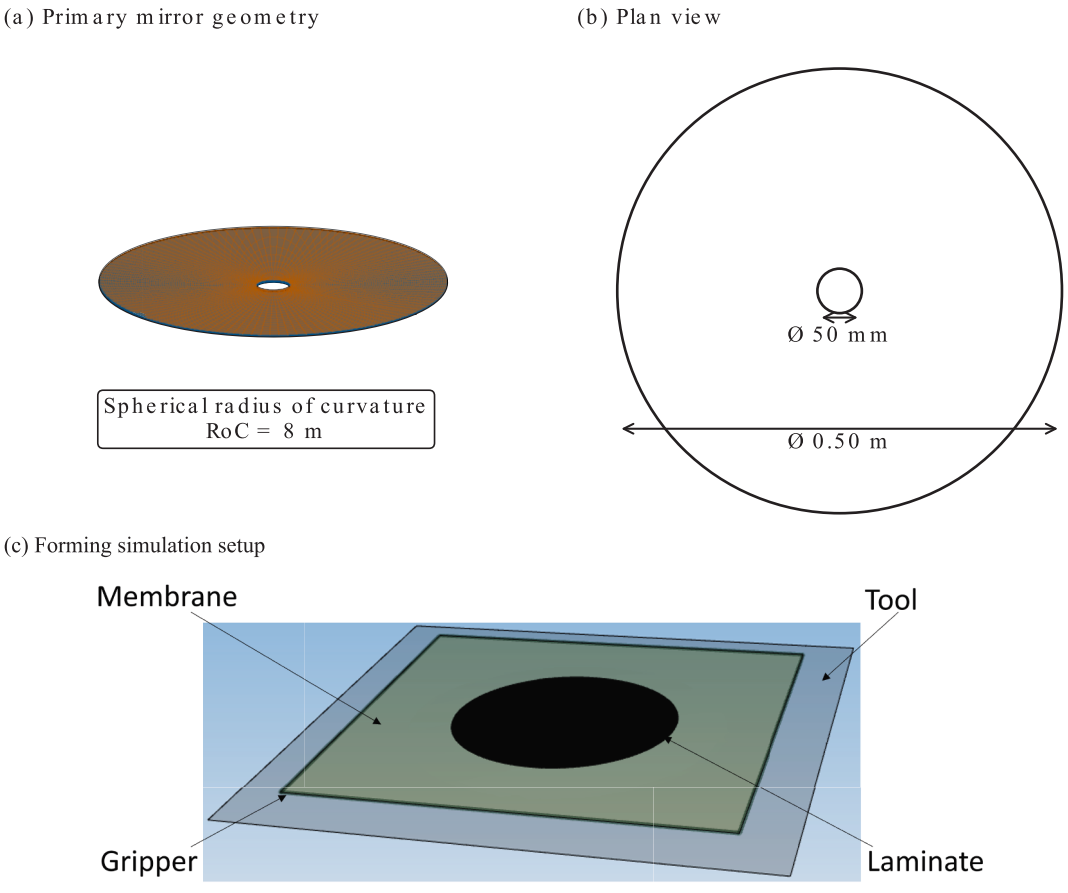


Fig. 1. Mirror geometry: (a) spherical dish (RoC = 8 m); (b) aperture view (D = 0.50 m, central aperture = 50 mm); (c) forming simulation setup showing rigid tool, membrane, and laminate configuration used for forming analysis.

assessment and the design criteria defined by the launch environment. Ply-level strength was evaluated using the Tsai–Wu failure index computed from in-plane stresses and lamina allowables. The Tsai–Wu criterion was selected as a widely used interactive failure criterion for multidirectional composite laminates and was employed here as a conservative laminate-level screening metric for in-plane strength assessment under launch loading. As shell elements were used, the analysis is limited to laminate-level in-plane stresses and does not resolve interlaminar or transverse normal (peeling) stresses. This provides a conservative first-level screening of in-plane failure risk under global loading. Interlaminar failure mechanisms (e.g., delamination), local contact effects at supports, and through-thickness stress concentrations were not modelled, as these require detailed 3D or contact submodelling and are outside the scope of the present laminate-level comparison.

3.2. Thermomechanical analysis

Thermoelastic deformation under representative in-orbit temperature extremes was evaluated using the same finite-element model and mesh as that used in structural analysis, with an operational three-point kinematic mount located at $r = 177$ mm. Each support was modelled by distributing constraints over a circular node set (20 mm radius) on the rear surface. This configuration restrains out-of-plane motion while allowing in-plane expansion, consistent with compliant mounting strategies used in precision optical systems. The associated reference points were fully fixed to ensure global stability.

Uniform temperature fields were applied to represent bounding hot (+125 °C) and cold (−65 °C) conditions relative to a 25 °C reference state. Ply-level coefficients of thermal expansion for the IM7/8552 carbon epoxy system were assigned at the lamina level (Table 1), and linear static analyses were performed to compute the resulting thermoelastic deformation. The assumption of spatially uniform temperature provides a controlled baseline for comparison, while neglecting in-orbit thermal gradients. Surface figure change was evaluated on the optical surface over the clear aperture using peak-to-valley (*PV*) and root-mean-square (RMS) out-of-plane displacement after removal of rigid-body motion. These metrics serve as first-order proxies for optical performance, enabling consistent comparison of deformation magnitude and spatial distribution between laminate concepts under identical conditions.

3.3. Hygrothermal analysis

Ground-to-orbit dimensional change due to moisture desorption was modelled as a worst-case transition from a moisture-saturated laminate to a fully dried state. For IM7/8552, the maximum equilibrium moisture uptake (0.39 wt% at 70 °C and 85% relative humidity) [32] was converted to an equivalent volumetric shrinkage using resin-dominated swelling/shrinkage relations, yielding an effective volumetric contraction of ~ 0.45%. This conversion assumes that moisture-induced mass uptake produces volumetric expansion proportional to resin swelling, i.e. $\Delta V/V \approx \beta \Delta M$, where β is an effective swelling coefficient for the matrix-dominated response.

Shrinkage was applied as a uniform eigenstrain at the homogenised lamina level. Isotropic contraction within each ply was assumed, consistent with the predominantly isotropic nature of resin swelling/shrinkage and its dominance over fibre response in moisture-driven volumetric change. Diffusion-driven gradients and transient effects were neglected to provide a controlled, comparable baseline between laminate concepts; this assumption isolates the influence of stiffness/thickness non-uniformity (e.g., RTS) on deformation and represents a conservative upper-bound case in which fully developed moisture gradients are not resolved. The analysis was implemented in Marc [33], using the same finite-element framework described in the chemo-thermomechanical analysis section, where full model details are provided. A first-order sensitivity indicates that reducing the applied shrinkage by ± 20% leads to proportional changes in RMS deformation without altering the relative ranking between laminate concepts. To suppress rigid-body motion without introducing artificial constraint stresses, a statically determinate minimal constraint scheme was adopted: one node fixed in all translational degrees of freedom ($u_1 = u_2 = u_3 = 0$), a second node constrained in $u_2 = u_3 = 0$, and a third node constrained in $u_3 = 0$. This configuration permits free global contraction while ensuring numerical stability.

3.4. Forming analysis

A forming simulation was performed in AniForm [34] to assess whether vacuum-assisted draping over the shallow spherical tool alters fibre orientations or introduces forming-related defect indicators. The primary objective was to verify preservation of the designed ply orientations during preforming. A unidirectional prepreg model representative of IM7/8552 was selected to capture the in-plane shear response governing drapability. The forming model comprised: (i) a rigid spherical tool extended to a rectangular clamping region; (ii) a deformable membrane; and (iii) an oversized circular 16-ply laminate corresponding to the structural stacking sequence (Fig. 1(c)). A single-membrane vacuum forming setup was assumed. Ply–tool and ply–ply contact interactions were defined, and forming loads included gravity, vacuum pressure, and prescribed membrane displacement toward the tool surface.

The primary outputs were fibre angle deviation and in-plane shear distribution, which were compared with the as-designed orientations to quantify forming-induced changes. Defect assessment was based on standard forming indicators (e.g., wrinkling, excessive shear, loss of contact), rather than explicit defect prediction. Given the shallow curvature of the mirror, the analysis focused on orientation preservation rather than forming limits. RTS-induced local thickness variations were not explicitly modelled, as drapability in such geometries is governed by in-plane shear deformation. Previous studies on tow-shearing processes have shown that shear deformation is the principal mechanism enabling fibre steering, while thickness variations arise as a secondary consequence of shear kinematics [6]. This represents a modelling simplification and should be interpreted as a limitation of the forming analysis.

3.5. Chemo-thermomechanical analysis

Manufacturing-induced residual stresses and geometric distortion arise during curing due to coupled heat transfer, cure kinetics, chemical shrinkage, and evolving resin stiffness [13]. In CHILE formulations, the composite is treated as incrementally linear elastic with properties evolving as functions of temperature and degree of cure. Although viscoelastic relaxation is not explicitly captured, CHILE has been shown to reproduce the dominant mechanisms governing cure-induced distortion in aerospace composites with good computational efficiency [35]. The coupled chemo-thermomechanical analysis was implemented in Marc [33] using user-defined subroutines. Cure kinetics, heat transfer, and cure-dependent material behaviour for IM7/8552 carbon/epoxy prepreg were incorporated through custom user subroutines, with full constitutive relations and parameters provided in Appendix A [36–39]. All model parameters were adopted directly from validated literature datasets for the IM7/8552 material system and were used predictively. This approach enables consistent coupling between thermal, chemical, and mechanical fields throughout the cure cycle.

A three-dimensional solid representation was adopted to resolve through-thickness gradients in temperature, degree of cure, and residual stress, which cannot be captured using shell elements. The Abaqus shell mesh used in thermomechanical and hypothermal analysis was converted into a layered solid mesh using a custom Python script (see Data Availability), with one solid layer per ply, consistent ply orientations, and thicknesses matching the structural model including RTS-induced

variation. The model employed eight-node composite brick elements (Marc element type 149 [40]) with two integration points per ply, providing adequate resolution of through-thickness behaviour. The cure simulation comprised two steps: (i) autoclave curing using the manufacturer-recommended IM7/8552 temperature cycle [27]; and (ii) constraint release (demoulding) implemented as a quasi-static step. The initial temperature was 25 °C, and the initial degree of cure was set to 0.05.

During cure, tool–part interaction was modelled as fully constrained (no slip), providing an upper-bound estimate of residual stress. This assumption represents a conservative limit; in practice, partial slip may occur depending on tooling and release conditions, which would reduce the magnitude of predicted distortion due to interfacial stress relaxation [13]. The dominant deformation modes are governed primarily by global laminate behaviour and cure shrinkage and are therefore not expected to change for differing tool-part conditions. After cooling, the mould constraint was released and replaced with a minimal three-node constraint scheme to suppress rigid-body motion while allowing free distortion. Cure-dependent composite properties were obtained using the Chamis micromechanics model, with temperature and cure dependence introduced through the resin phase while fibre properties were assumed constant [41]. Chemical shrinkage was modelled as an incremental eigenstrain linked to degree-of-cure evolution, based on the Johnston–Hubert volumetric shrinkage model [36], and mapped to orthotropic composite strains using micromechanical relations (Appendix A).

3.6. Optimisation and sensitivity analysis

A multi-objective optimisation framework was developed to minimise (i) areal density and (ii) surface deformation (RMS) of the mirror while satisfying launch and operational constraints. All candidate laminates were evaluated using identical finite-element models, boundary conditions, and load cases to ensure direct comparability. Design feasibility was enforced using three constraint sets. First, the fundamental frequency was required to exceed 140 Hz, consistent with typical spacecraft design practice to avoid coupling with launch vehicle excitation and to ensure sufficient dynamic stiffness [23]. Second, the maximum Tsai–Wu failure index across all plies and elements was limited to < 0.5, providing a conservative margin against in-plane failure under combined launch loads and accounting for uncertainties in material properties and loading. Third, the total ground-to-orbit figure change was constrained by limiting the combined thermal and hygroscopic distortion (RMS) within the allowable optical budget. Candidate solutions were evaluated in an FE-in-the-loop framework and ranked using non-dominated sorting to identify Pareto-optimal designs defining the mass–distortion trade space.

For straight-fibre laminates, designs were restricted to balanced and symmetric layups to eliminate membrane–bending coupling and ensure manufacturability. Two quasi-isotropic families, [0/90/±45] and [0/90/±45/±30/±60], defined the initial design space. In an initial stage, cured ply thickness was treated as a continuous variable and different objective metrics (maximum, mean, and RMS displacement) were explored. Following this preliminary investigation, ply thickness was fixed and the optimisation focused on ply-angle selection within balanced symmetric layups. Candidate laminates were evaluated using the optimisation framework described previously and ranked according to the objective functions and design constraints. The resulting optimal laminate configurations and their performance are presented and discussed in Section 4.2.

RTS optimisation was based on a quasi-isotropic baseline $[45/-45/90/0]_S$, with spatially varying fibre paths introduced as additional design variables. Each steered ply was defined along a 600 mm reference path with control points at 100 mm intervals, with fibre angles linearly interpolated between control points. Balance and symmetry were enforced by pairing each steered ply with its mirrored counterpart. RTS-induced thickness variation from shear–thickness coupling was retained, such that laminate mass emerged as an optimisation outcome rather than a prescribed parameter.

Five RTS configuration families (A–E), which are summarised in Table 2, were considered, differing in the set of plies allowed to steer. Configuration A did not satisfy the frequency constraint and was discarded. For the remaining families, increasing steering freedom reduced thermal distortion (RMS) but increased mass due to local tow thickening. Configurations B–D were therefore evaluated at multiple steering amplitudes, while configuration E prioritised steering in 0° and 90° plies. The resulting design space defines the mass–distortion trade-off used for selection of representative laminates for detailed analysis.

3.7. Manufacturing feasibility and process

A manufacturability assessment was conducted to verify that the optimised RTS fibre paths are compatible with practical placement constraints and do not require tight local steering. The mirror was manufactured from IM7/8552 carbon/epoxy prepreg [28], selected for its high specific stiffness and low in-plane CTE. Fig. 2 shows the spatial fibre-orientation fields for the steered plies and their mirrored counterparts. The orientation fields vary smoothly across the aperture, and through-thickness symmetry is maintained to avoid unintended bending–extension coupling. Fibre orientation is defined relative to the global laminate coordinate system used in the structural model.

Manufacturability was quantified by extracting fibre angles along predefined reference paths (Fig. 3) and converting the spatial variation into equivalent steering radii. Steering radii were used as manufacturability indicators to assess compliance with RTS placement constraints. The resulting steering angles and radii are summarised in Table 3 and are evaluated in Section 4.2 as part of the design-selection process.

Mirrors were manufactured using an RTS process chain comprising flat preform deposition, vacuum-assisted forming, and autoclave curing. Preforms were deposited on a flat tool with typical placement tolerances of ± 2° in fibre angle and ± 1 mm in tow position. The central aperture was machined after deposition to avoid fibre discontinuities within the optical region. Placement quality was verified by image-based inspection to confirm fibre-angle fidelity and absence of visible defects. Forming was performed by vacuum-assisted draping onto a precision Invar tool. Active forming was not required due to the shallow curvature, consistent with the results of forming simulations. The tool was manufactured with a nominal radius of 8001 mm with an approximate geometric deviation of ± 2 mm based on metrology measurements, an RMS figure deviation of ~ 13–15 μm after thermal cycling, and a surface roughness of $R_a \approx 0.8$ μm [42].

Consolidation followed standard aerospace vacuum-bagging practice (Fig. 4). Autoclave curing followed the manufacturer-recommended IM7/8552 cycle [27], with slightly extended dwell times by approximately 10 min to compensate for measured thermal lag. A pressure of 6.5 bar and full vacuum were applied to ensure consistent compaction.

Table 2
Laminate configurations considered: straight-fibre (S1–S2) and RTS (A–E).

Configurations	Stacking sequence (symmetric laminates)
S1	$[60/-60/30/-30/0/90/45/-45]_S$
S2	$[0/90/45/-45]_{2s}$
A	**[45/45*/−45/−45*/0/90/90/0/−45*/−45/45*/45]**
B1 & B2	**[45/45*/−45/−45*/0/90/0/90/90/0/90/0/−45*/−45/45*/45]**
C1 & C2	**[45/45*/−45/−45*/90/0/0*/90/90/0*/0/90/−45*/−45/45*/45]**
D1 & D2	**[45/45*/−45/−45*/90/0/0*/90*/90*/0*/0/90/−45*/−45/45*/45]**
E	**[45/45*/−45/−45*/0/0*/90/90/0*/0/−45*/−45/45*/45]**

Boldface identifies RTS plies (plies where fibre paths are steered).
The asterisk (*) indicates duplicate plies used to maintain laminate symmetry.

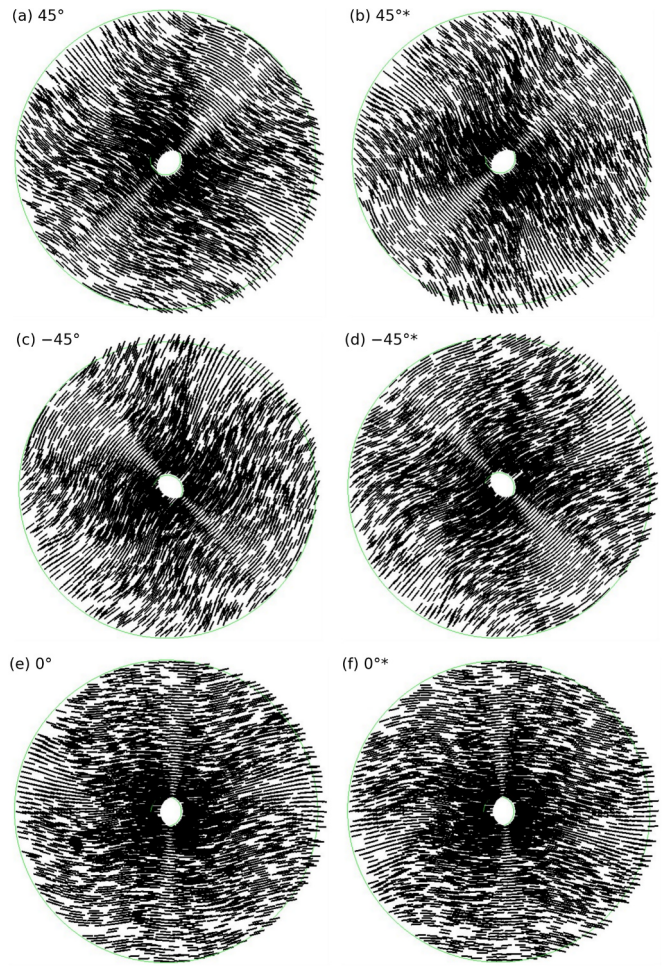


Fig. 2. Orientation distributions for RTS plies showing fibre paths (1-axis direction): (a) 45°, (b) 45°*, (c) –45°, (d) –45°*, (e) 0°, (f) 0°*.

These parameters were selected to achieve repeatable consolidation and minimise process-induced variability. The manufactured straight-fibre and RTS mirrors are shown in Fig. 5.

3.8. Experimental characterisation

The structural and thermoelastic behaviour of the straight-fibre and RTS mirrors was evaluated using complementary techniques targeting: (i) global surface figure; (ii) local surface quality; (iii) thermally induced deformation; and (iv) material state and mechanical performance. Global surface geometry was measured using a Leica Absolute Tracker AT901 [43] with a T-Probe. Each mirror was supported on a rigid annular ring with a compliant silicone interlayer to minimise constraint influence. Measurements were acquired over the clear aperture using radial scanning paths, and point clouds were registered to the nominal spherical geometry. Surface deviations were quantified using RMS error and annular Zernike polynomial decomposition, after removal of piston, tilt, and defocus [44]. This approach enables separation of low-order (global) and higher-order surface errors relevant to optical performance. Local surface roughness was characterised at the centre and mid-radius using a Form Talysurf 120 L profilometer [45]. Multiple traces were acquired over a 40 mm evaluation length, and profiles were levelled and filtered to separate waviness from roughness. Roughness

Table 3
Steering angles and radii for all RTS plies (0°, ±45°).

Control Point	0° Plies – Steering Angle (°)	0° Plies – Steering Radius (mm)	±45° Plies – Steering Angle (°)	±45° Plies – Steering Radius (mm)
θ_0/R_1	5.18	440.02	2.49	813.63
θ_1/R_2	18.78	207.79	9.33	164.85
θ_2/R_3	−9.52	371.96	−26.30	212.84
θ_3/R_4	5.90	262.72	1.18	220.16
θ_4/R_5	−16.46	948.32	−25.26	806.29
θ_5/R_6	−10.08	204.49	−16.25	173.20
θ_6	18.31	—	17.55	—

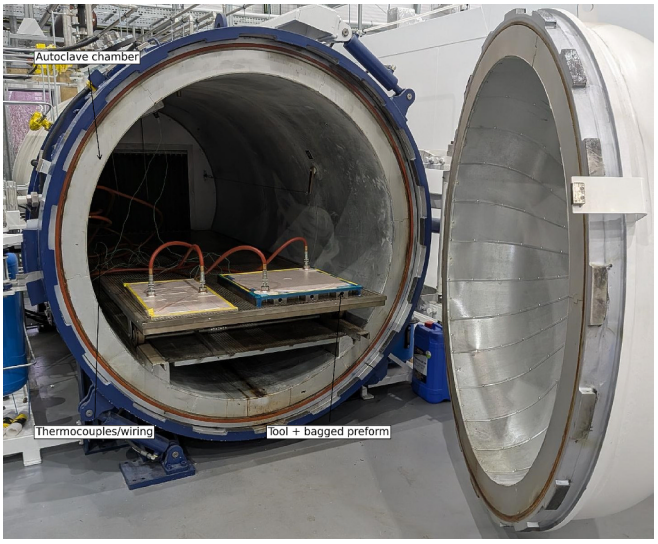


Fig. 4. Autoclave curing of vacuum-bagged preform.

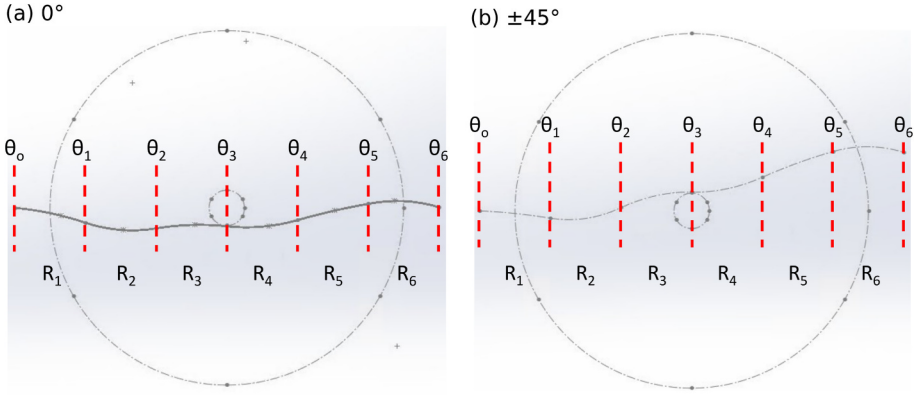


Fig. 3. Spatial distribution of steering angles and radii for RTS plies: (a) 0° plies, (b) ± 45° plies.

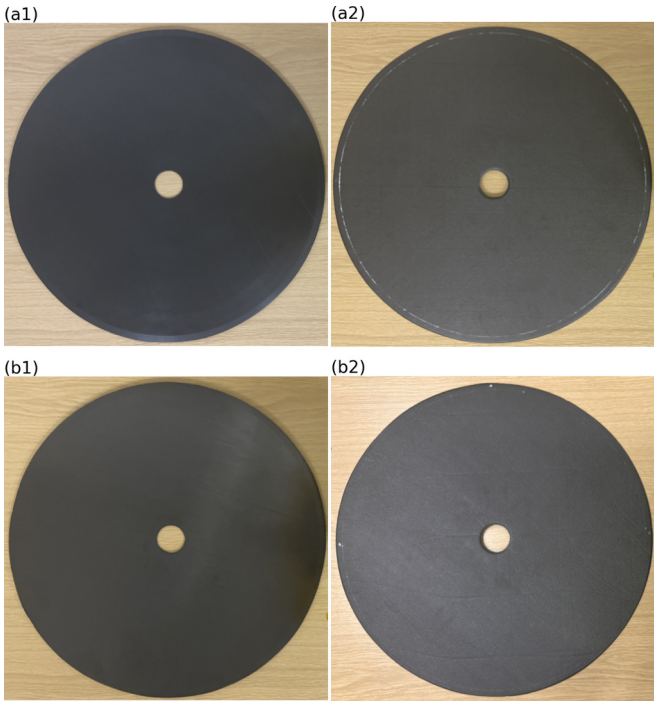


Fig. 5. Manufactured composite reflectors: straight-fibre laminate (a1) optical side, (a2) non-optical side; RTS laminate (b1) optical side, (b2) non-optical side.

parameters were evaluated in accordance with ISO 4287 [46].

Thermomechanical deformation was measured using a Hexagon Absolute Scanner AS1 [47]. Mirrors were heated from approximately 20 °C to 120 °C using a hot plate with a copper powder interface (Polycraft copper powder, MB Fibreglass, UK; nominal purity ≥ 99%, fine particulate grade) to ensure uniform thermal contact while minimising constraint (experimental setup shown in Fig. 6). A measured in-plane temperature gradient of ~ 20 °C was present, introducing additional deformation components not captured in the uniform-temperature simulations. Full-field surface scans were acquired at both temperature states, and datasets were processed through down-sampling, outlier removal, and sphere fitting. Zernike decomposition (up to radial order 6) was applied to quantify residual deformation. The measurement accuracy (on the order of tens of micrometres) is sufficient to resolve dominant deformation modes and support comparison with modelling trends. The measurement accuracy of the Leica AT901 and Hexagon AS1 systems is approximately 10–30 μm based on instrument specifications and repeatability assessments. This uncertainty is sufficient to resolve the dominant deformation modes and support comparison with modelling trends. To ensure robustness, three repeated scans were acquired at each thermal condition and averaged. Measurement uncertainty (≈10–30 μm) is small relative to the dominant global deformation (≈100–300 μm *PV*) but is comparable to higher-order residuals; therefore, the analysis focuses on trends in low-order modes and relative changes rather than absolute small-amplitude differences.

Following non-destructive evaluation, destructive testing was conducted to assess material quality and mechanical behaviour. Cure uniformity was evaluated using DSC on samples extracted from multiple radial locations. Glass transition temperature (T_g) and residual enthalpy were measured, with spatial consistency indicating uniform cure across the aperture. Mechanical performance was assessed using three- and four-point bending tests (ASTM D7264, $n = 5$ per configuration) on coupons extracted from the mirrors. Tests were conducted with standard span-to-thickness ratios (32:1 for both three- and four-point bending), with load–displacement data obtained from crosshead displacement and properties calculated according to the standard. In addition, unidirectional IM7/8552 laminates (16 plies) were tested to provide a material baseline. Interlaminar shear strength (ILSS) was measured using short-beam testing (ISO 14130) [48] to characterise matrix-dominated behaviour. Microstructural analysis using optical microscopy was performed to identify failure mechanisms and potential defects. These tests provide material-level validation and enable comparison of stiffness and strength between straight-fibre and RTS laminates.

4. Results

4.1. Forming feasibility

A membrane-assisted vacuum forming simulation was performed to evaluate whether draping the straight-fibre laminate over the shallow spherical tool affects fibre orientation or introduces forming-related defects. Fibre reorientation across all plies was negligible, with a maximum deviation of 0.0052° and an average of 0.0045°, which is orders of magnitude smaller than typical placement tolerances (±2°), confirming that the designed fibre orientations are effectively preserved during forming. More than 85% of elements exhibited deviations below 0.01%, indicating no significant reorientation. Forming simulations also indicated no evidence of defect indicators such as wrinkling, excessive shear, ply slippage, or loss of tool contact, with full contact maintained throughout the process. These results demonstrate that forming has a negligible influence on laminate architecture and does not affect the structural or thermoelastic response for the present shallow-curvature geometry. Given that forming-induced orientation changes are negligible relative to the designed fibre variations in RTS laminates, forming was not re-simulated for the RTS configuration. This assumption implies that RTS thickness variation has a negligible influence on drapability for the present shallow-curvature geometry and is treated as a modelling simplification.

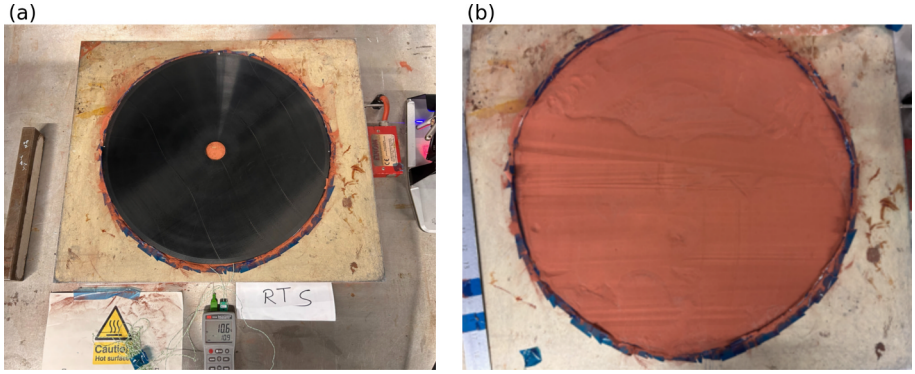


Fig. 6. Thermomechanical test setup: (a) mirror on hot plate; (b) copper powder interface for improved thermal contact and minimal constraint.

4.2. Final design selection

The optimisation studies described in Section 3.6 showed that the straight-fibre design space consistently favoured near-quasi-isotropic laminate configurations. Continuous thickness optimisation produced only minor thickness variations and limited improvement in performance, indicating that thickness optimisation offered little practical benefit. Subsequent angle optimisation of balanced symmetric laminates identified [0/90/±45] and [0/±60]-type configurations as the most favourable solutions when thermoelastic and hygroscopic responses were considered simultaneously. Manufacturability assessment of the RTS configurations showed a minimum steering radius of approximately 165 mm, with most steering radii exceeding 200 mm, confirming compatibility with RTS placement constraints. The final laminate selection was therefore based on these candidate configurations together with the RTS design families described in Section 3.6.

A trade-off study was conducted to select representative straight-fibre and RTS mirror laminates for detailed analysis. Candidate designs were compared using five attributes: ply count, mass, thermoelastic distortion, hygroscopic distortion, and cure-induced distortion, as summarised in Table 4. Overall ranking was obtained using a weighted sum, where lower mass and distortion correspond to more favourable scores. Thermoelastic distortion was assigned the highest weight, as it acts continuously in orbit. Hygroscopic distortion was assigned a smaller weight, as moisture loss occurs primarily during early mission exposure and can be partially compensated. Cure-induced distortion was assigned the lowest weight, since it is dominated by low-order modes and can be mitigated through tool compensation and process optimisation. Ply count was included separately to reflect manufacturing complexity and risk.

For the straight-fibre baseline, two quasi-isotropic laminates (S1 and S2) were evaluated. Both exhibited identical mass (0.644 kg) and nearly identical thermoelastic distortion (~69 μm RMS), indicating that thermoelastic response is insensitive to the stacking-sequence variations considered. S2 produced slightly lower hygroscopic distortion (16.7 μm vs 17.1 μm) but higher cure distortion. Based on the selected weighting, S2 ($[0/90/45/–45]_{2S}$) was marginally preferred and selected as the baseline design.

RTS candidates (families B–E) exhibited thermoelastic distortion within a narrow range (~66–68 μm RMS), comparable to the straight-fibre designs despite the thickness variation. Consequently, ranking was primarily governed by mass and ply count. Configuration E achieved the lowest mass (0.578 kg, 14 plies) while maintaining comparable thermoelastic performance. This reduction was accompanied by increased hygroscopic (22.7 μm RMS) and cure distortion (98.4 μm RMS), reflecting the influence of spatial stiffness and thickness variation introduced by fibre steering. Based on the ranking, the two designs selected for detailed evaluation were straight-fibre configuration S2 $[0/90/45/–45]_{2S}$ and RTS configuration E [**45/45*/—45/—45*/0/0***/90/90/**0*/0/—45*/—45/45*/45**]. Here, steered (RTS) plies are identified in bold in Table 2, and "*" denotes the mirrored duplicate plies required to maintain laminate symmetry. Hereafter, these are referred to as "straight-fibre" and "RTS", respectively.

Table 4
Trade study results for straight-fibre (S1–S2) and RTS (B1–E) mirror configurations.

Configuration	Plies	Mass (kg)	Thermal (μm)	Hygroscopic (μm)	Cure (μm)	Weighted score
S1	16	0.644	69.28	17.1	83.5	−11.711
S2	16	0.644	69.28	16.7	89.2	**−11.696**
B1	16	0.648	68.61	18.9	97.3	−11.751
B2	16	0.650	68.11	20.9	91.3	−11.797
C1	16	0.653	68.32	21.0	83.5	−11.819
C2	16	0.667	67.37	22.1	87.9	−11.797
D1	16	0.668	66.06	20.5	94.7	−11.594
D2	16	0.671	65.94	20.4	94.4	−11.579
E	14	0.578	67.81	22.7	98.4	**−11.392**

4.3. Launch stiffness and strength performance

Both mirror designs achieve low areal density while satisfying the launch stiffness requirement of a first natural frequency above 140 Hz. The straight-fibre laminate has an areal density of 3.31 $kg{\cdot}m^{-2}$, whereas the RTS laminate achieves 2.97 $kg{\cdot}m^{-2}$, corresponding to an ~ 11% mass reduction. The straight-fibre mirror has a uniform thickness of approximately 2.10 mm (16 plies), while the RTS mirror exhibits a spatial thickness variation (≈1.83–1.96 mm) due to shear–thickness coupling (Fig. 7). Despite this non-uniformity, both designs satisfy the dynamic requirement, with first-mode frequencies of ~ 153 Hz (straight-fibre) and ~ 145 Hz (RTS). This demonstrates that RTS can reduce mass while maintaining sufficient global stiffness.

Strength under launch loading was evaluated using the maximum Tsai–Wu failure index as a first-level in-plane screening metric. Tsai–Wu was selected as a conservative interactive criterion suitable for laminate-level assessment, rather than detailed failure prediction. A limit of 0.5 was adopted to provide a conservative margin relative to the nominal failure envelope. Under 15 g axial acceleration, peak indices were 0.011 (straight-fibre) and 0.013 (RTS), indicating large safety margins relative to the allowable limit (0.5). Under 4 g lateral loading, indices were on the order of 10^{-4}, confirming that lateral loading is non-critical. Peak values are localised near support regions (Fig. 8), while most of the aperture experiences low stress levels. Interlaminar stresses and local contact effects at supports were not considered and would require higher-fidelity 3D modelling; therefore, the results should be interpreted as laminate-level screening rather than a complete failure assessment.

Random vibration was approximated using a static-equivalent axial acceleration derived from the Miles relation [31], based on a representative NASA qualification PSD profile (0.026 g^2/Hz at 20 Hz, increasing to 0.16 g^2/Hz between 50–800 Hz, and decreasing to 0.026 g^2/Hz at 2000 Hz). A transmissibility factor of $Q = 25$ (≈2% damping) and dominant first-mode response were assumed. The resulting equivalent accelerations were ~ 93 g for the straight-fibre mirror and ~ 91 g for the RTS mirror, yielding maximum Tsai–Wu indices of ~ 0.07 and ~ 0.08, respectively, indicating substantial strength margins relative to the allowable limit (Fig. 9). This static-equivalent approach is intended for preliminary screening rather than formal qualification. Overall, launch stiffness requirements govern the design, while in-plane strength is non-critical for both laminate concepts. It is noted that this assessment does not include interlaminar failure, transverse normal (peeling) stresses, local contact effects, or manufacturing defects, and should therefore be interpreted as a first-level in-plane screening rather than a complete qualification analysis.

4.4. Thermoelastic distortion

Thermoelastic deformation was evaluated under uniform temperature excursions using a compliant three-point mount that allows in-plane expansion. The straight-fibre mirror exhibits RMS out-of-plane displacements of ~ 69.3 μm (hot) and ~ 62.4 μm (cold), while the RTS mirror shows comparable values (~67.8 μm and ~ 61.0 μm, respectively). These results indicate that both laminate concepts exhibit similar thermoelastic performance at the global (RMS) level.

In contrast, peak displacements in the hot case are higher for the RTS mirror, reaching ~ 121 μm compared to ~ 96 μm for the straight-fibre design (Fig. 10). These localised increased values arise from spatial variations in stiffness and thickness introduced by fibre steering, which generate additional non-axisymmetric curvature components. Despite these local differences, the RMS deformation remains similar to that of the straight fibre case, indicating that thermoelastic response is primarily governed by laminate-level properties, particularly effective CTE and global bending stiffness, rather than local stiffness tailoring. As a

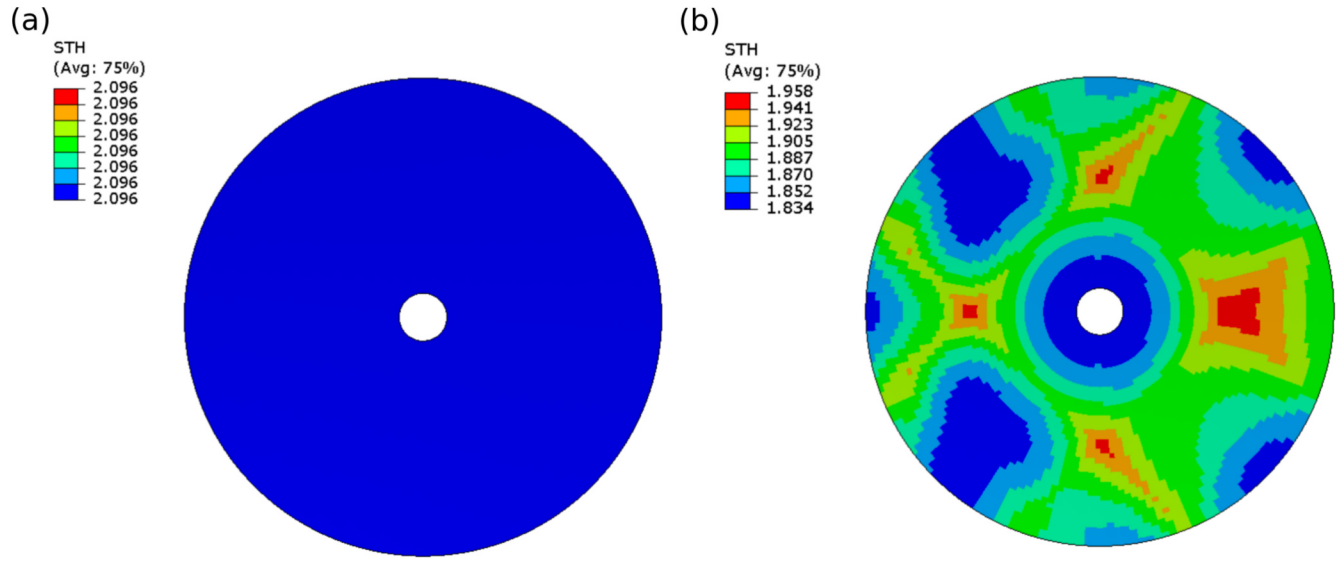


Fig. 7. Laminate thickness: (a) straight-fibre (uniform 2.096 mm); (b) RTS (1.834–1.958 mm due to tow shearing), shown as a colourmap in mm.

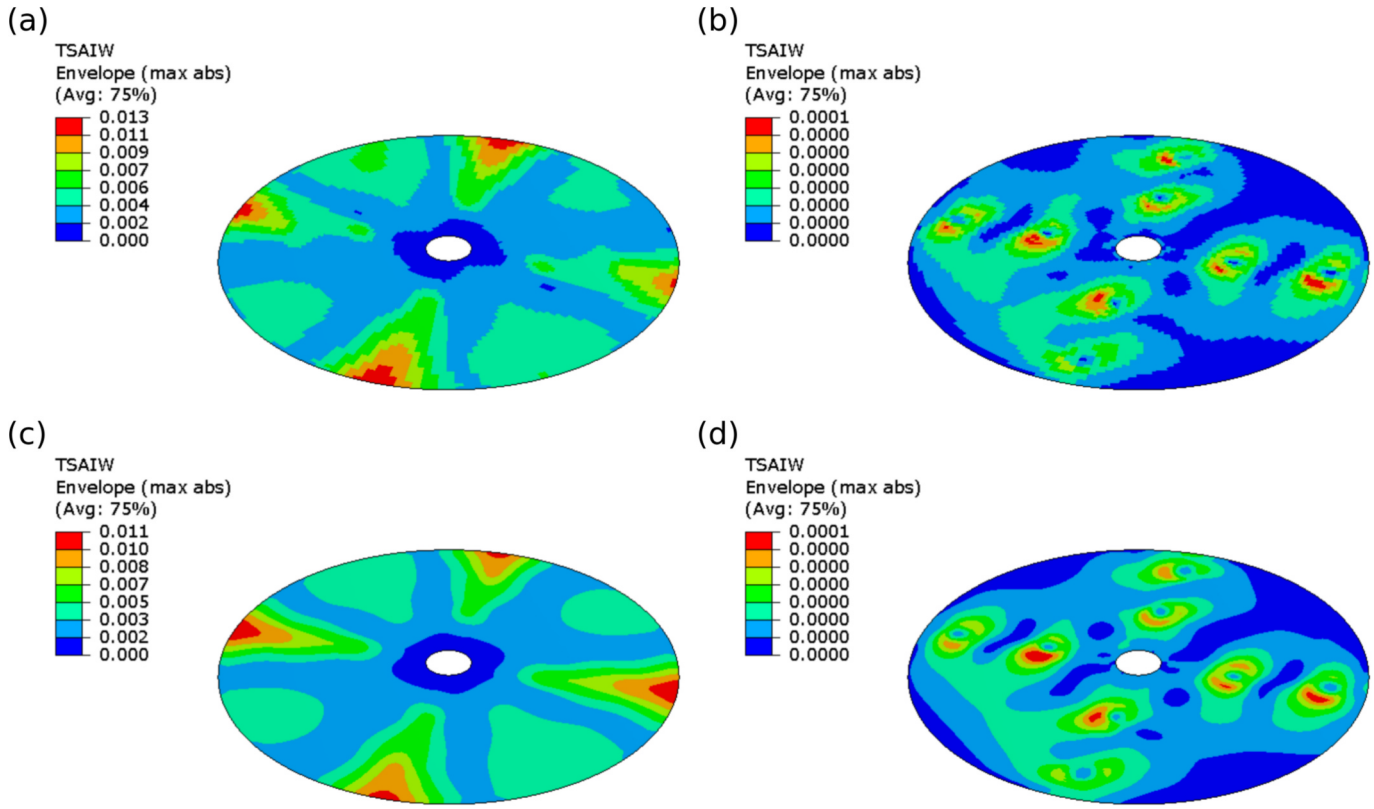


Fig. 8. Tsai–Wu failure index under launch quasi-static accelerations: (a) straight-fibre, 15 g axial; (b) straight-fibre, 4 g lateral; (c) RTS, 15 g axial; (d) RTS, 4 g lateral.

result, RTS does not significantly reduce global thermoelastic distortion under uniform temperature loading. The deformation fields for both laminates are dominated by smooth, low-order modes, with maximum displacement occurring toward the outer annulus (Fig. 10). This behaviour is characteristic of thermally induced curvature change and suggests that figure error is governed by global deformation rather than high-frequency surface features. Overall, RTS achieves comparable thermoelastic stability at reduced mass but introduces increased local peak deformation due to stiffness non-uniformity, without altering the dominant deformation mechanisms.

4.5. *Hygroscopic distortion*

Moisture-related dimensional change was evaluated by applying a uniform volumetric shrinkage of 0.45%, representing moisture desorption during the ground-to-orbit transition. The predicted hygroscopic distortion is smaller than the thermoelastic response, yielding ~ 16.7 μm RMS for the straight-fibre mirror and ~ 22.7 μm RMS for the RTS mirror.

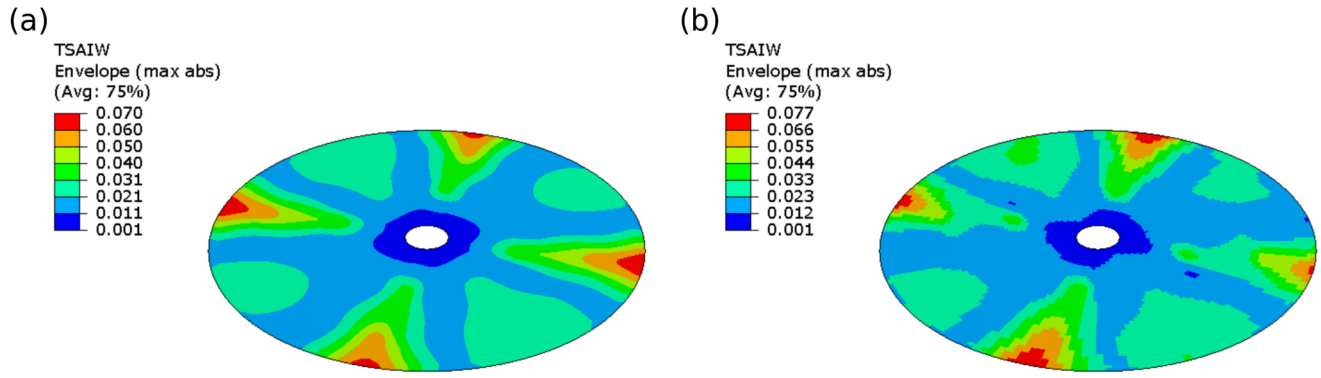


Fig. 9. Random vibration (static-equivalent axial) strength assessment: (a) straight-fibre at 152.72 Hz with equivalent ~ 93 g (max Tsai–Wu ≈ 0.07); (b) RTS at 145.02 Hz with equivalent ~ 90.55 g (max Tsai–Wu ≈ 0.08).

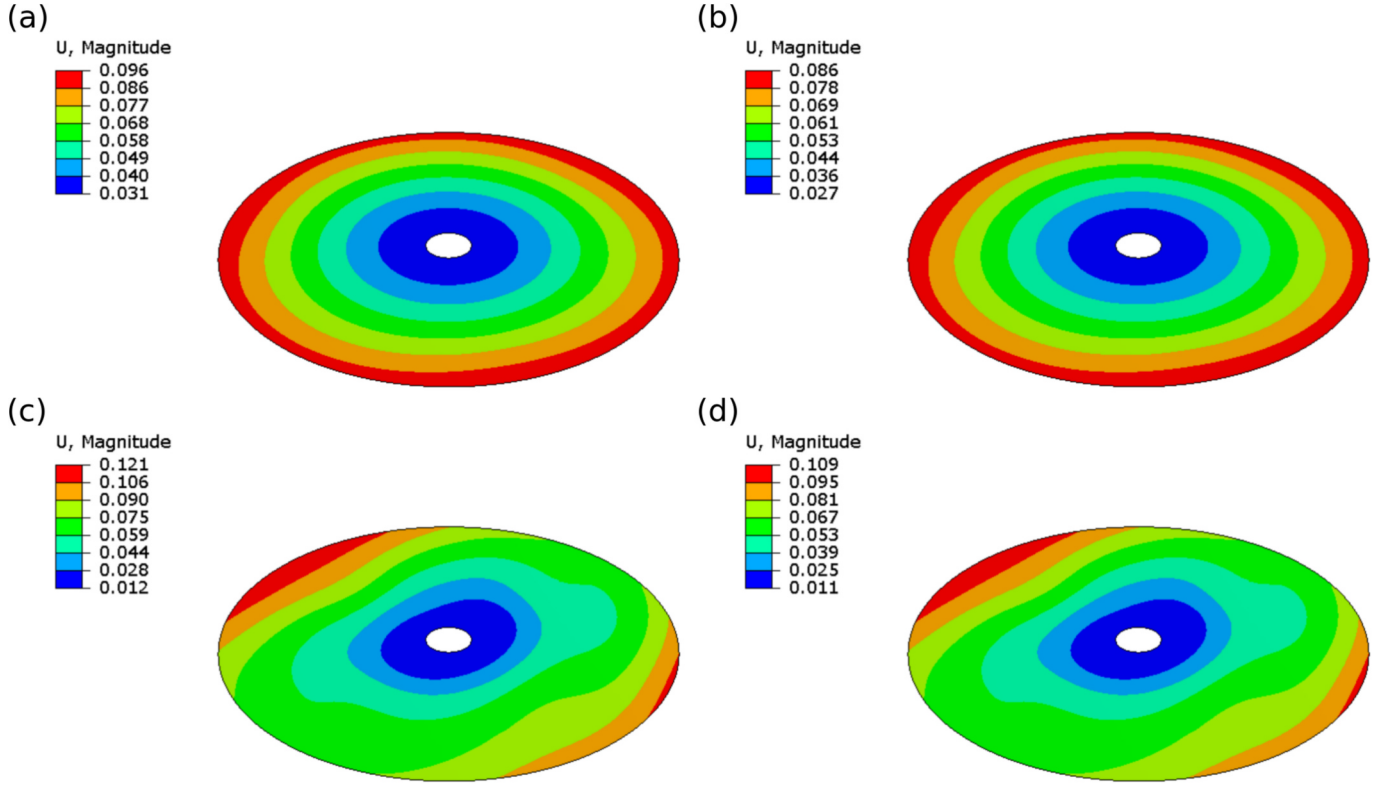


Fig. 10. Out-of-plane displacement (mm) under uniform temperature change: straight-fibre (a) hot, (b) cold; RTS (c) hot, (d) cold.

This indicates that hygroscopic effects are secondary but more sensitive to laminate non-uniformity. The straight-fibre laminate exhibits a smooth and largely axisymmetric deformation pattern, with a maximum displacement of ~ 23.8 μm (Fig. 11a). In contrast, the RTS laminate shows a more spatially non-uniform deformation field, with a higher peak displacement of ~ 36.5 μm (Fig. 11b). This increased non-uniformity arises from the interaction between uniform shrinkage strain and spatial variation in stiffness and thickness introduced by fibre steering.

Although the difference in RMS values is modest, the RTS laminate shows increased sensitivity to shrinkage-induced deformation, resulting in both higher RMS and peak displacement. This behaviour highlights that stiffness non-uniformity amplifies deformation under uniform eigenstrain loading. It is noted that this analysis represents a conservative, instantaneous shrinkage case. In practice, moisture desorption is time-dependent and may introduce transient gradients and additional deformation modes, which are not captured in the present model.

4.6. *Cure-induced distortion*

Coupled CHILE-based chemothermal simulations predict significant cure-induced distortion for both designs, with maximum out-of-plane displacements of approximately 184 μm (straight-fibre) and 210 μm (RTS) (Fig. 12). The corresponding RMS values are approximately ~ 90 μm for the straight-fibre laminate and ~ 98 μm for the RTS laminate, indicating comparable global deformation levels. The straight-fibre laminate exhibits predominantly axisymmetric deformation (global doming), whereas the RTS laminate shows increased non-axisymmetric warpage and slight tilt, consistent with spatial variation in stiffness and thickness introduced by fibre steering.

Despite the larger magnitude compared to thermoelastic deformation, cure-induced distortion is dominated by low-order modes, primarily curvature change, and is reflected in both peak and RMS values. As a result, the deformation manifests mainly as a shift in radius of curvature rather than high-frequency surface error, meaning that low-

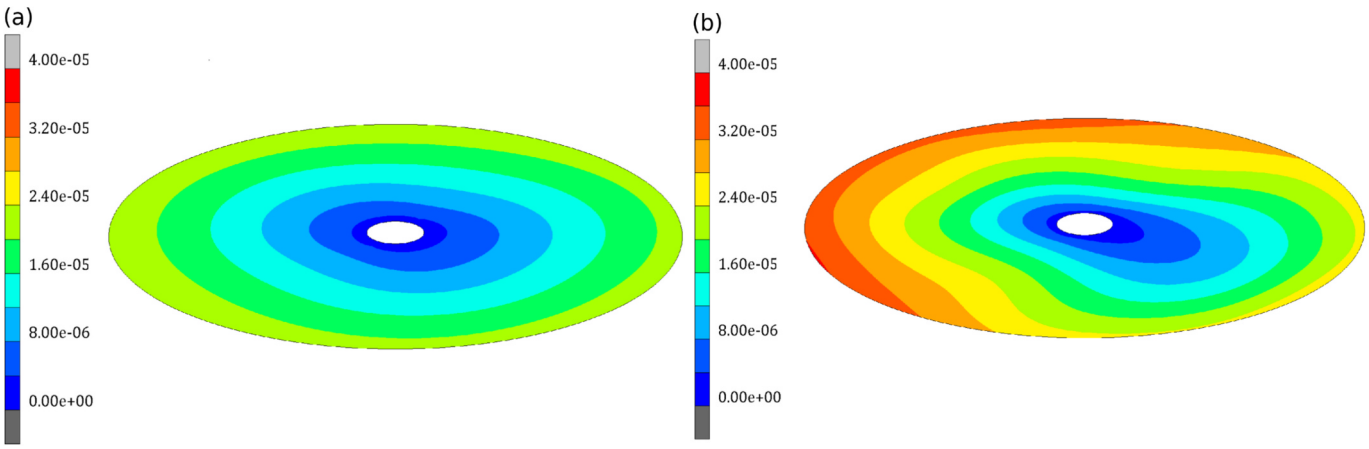


Fig. 11. Moisture-desorption deformation fields (m): (a) straight-fibre; (b) RTS.

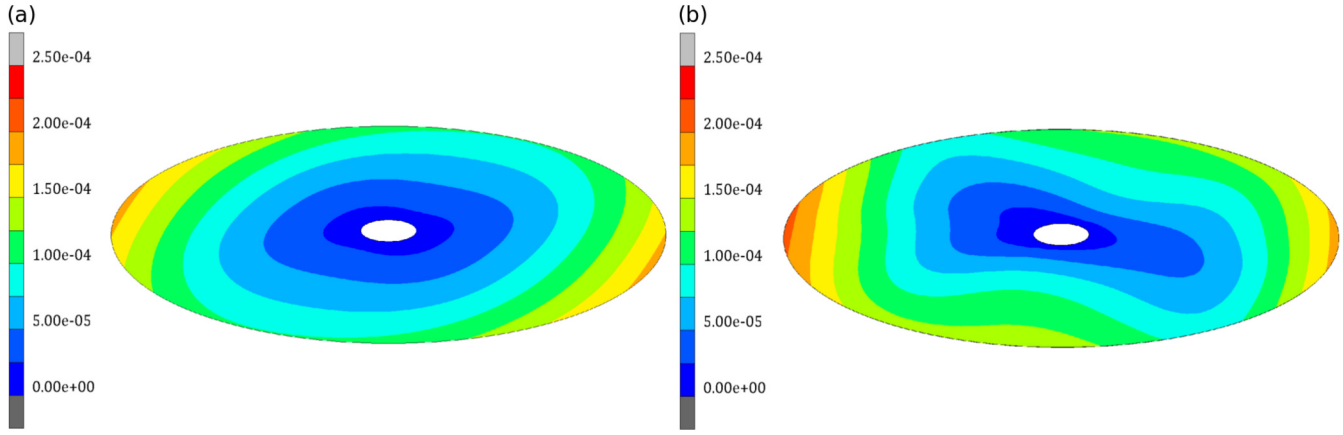


Fig. 12. Predicted post-demoulding distortion from CHILE simulations (m): (a) straight-fibre; (b) RTS.

order errors can be mitigated through tool compensation or process optimisation. The RTS laminate exhibits slightly higher deformation due to its non-uniform stiffness and thickness distribution, which alters residual stress development during cure and cool-down; however, the difference between the two designs remains modest, indicating that cure-induced distortion is governed primarily by global laminate behaviour and processing conditions rather than local fibre steering effects. It is noted that the modelling assumption of a fully constrained tool during cure represents an upper-bound condition for residual stress development. While RTS introduces increased asymmetry, cure-induced effects remain secondary to thermoelastic behaviour in determining in-service figure stability.

4.7. Experimental validation

To facilitate comparison between modelling and experimental observations, Table 5 summarises the principal numerical predictions and corresponding experimental findings for the straight-fibre and RTS mirrors. The objective is not to provide a point-by-point quantitative validation, since the experiments include residual stresses, thermal gradients and support effects that are not represented in the thermo-elastic simulations, but rather to compare dominant deformation modes and relative trends. Experimental validation focused on surface geometry, thermo-mechanical response, and material properties to assess the consistency of the predicted deformation mechanisms. Surface figure was evaluated as out-of-plane deviation from a spherical reference after removal of rigid-body motion. Two fitting approaches were used: a fixed-radius sphere (tool radius) and a best-fit sphere with optimised radius (Table 6). This separation enables a distinction between global curvature change and higher-order residual deformation. To isolate non-spherical content, measured surfaces were decomposed into annular Zernike polynomials (up to radial order $N \leq 6$) after removal of piston, tilt, and defocus (Fig. 13). The residual RMS was 49.1 μm for the straight-fibre mirror and 58.5 μm for the RTS mirror, representing

Table 5
Comparison between modelling and experiment.

Metric	Model	Experiment
Dominant mode	Low-order	Low-order
Straight-fibre RMS (μm)	~69	49
RTS RMS (μm)	~68	59
RTS effect	Lower mass, similar RMS	Increased asymmetry
Thermal response	Global curvature change	Residual-stress relaxation

Table 6
Sphere-fitting results for measured mirror surfaces.

Metric	Tool (reference)	Straight-fibre (fixed R)	Straight-fibre (best-fit)	RTS (fixed R)	RTS (best-fit)
Fitted sphere radius (mm)	8063.9	8063.9	8277.35	8063.9	8283.2
Peak-to-valley error (μm)	77.9	937	931	494	520
RMS error (μm)	14.9	180.0	178.3	104	99.7

Fixed R: radius constrained to tool value (8063.9 mm). Best-fit: radius optimised during fitting.

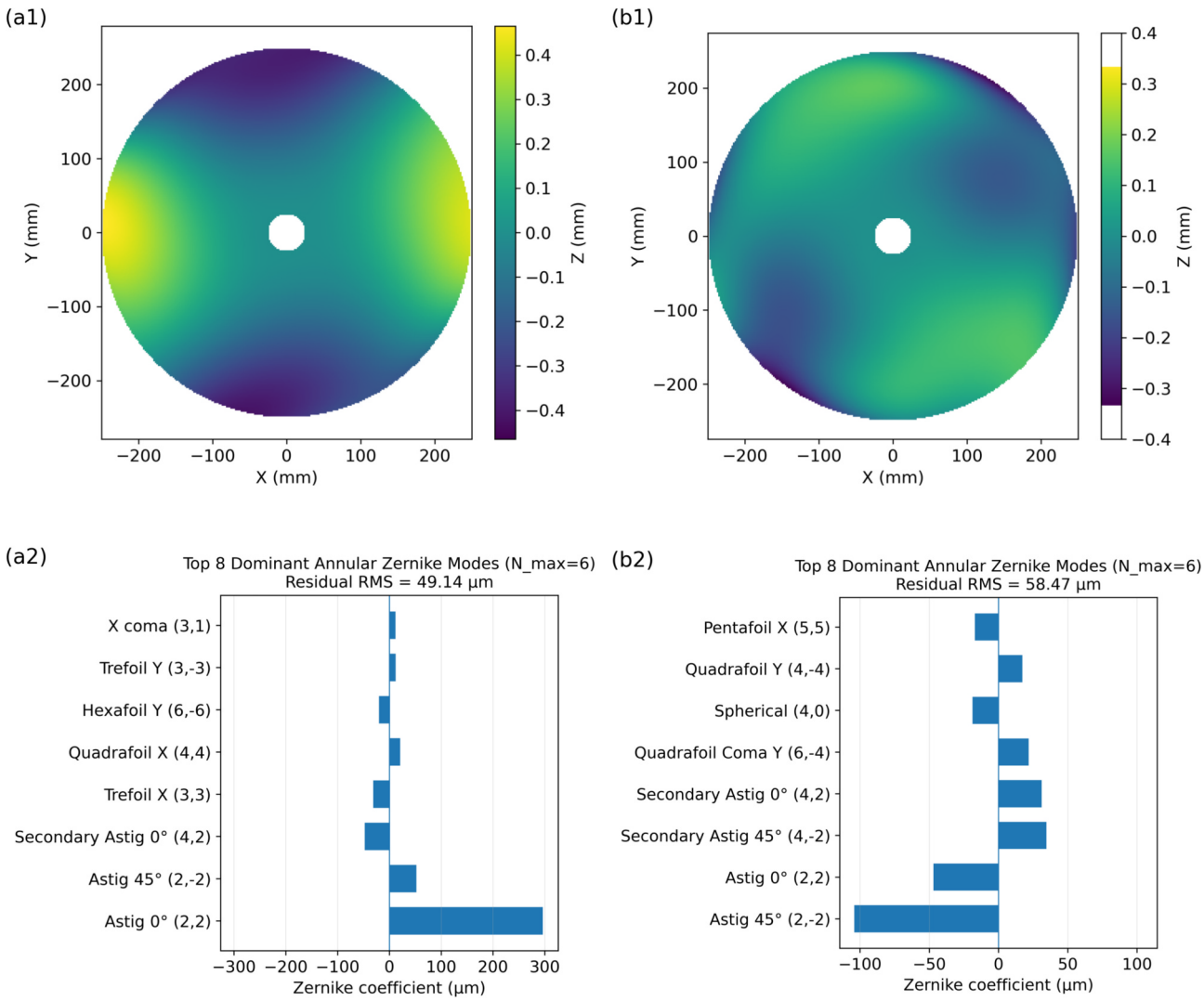


Fig. 13. Residual surface after removing piston, tilt, and defocus: (a1) straight-fibre, (b1) RTS; dominant annular Zernike terms: (a2) straight-fibre, (b2) RTS.

higher-order and non-axisymmetric components. The straight-fibre mirror exhibits predominantly axisymmetric behaviour, whereas the RTS mirror shows increased non-axisymmetric contributions, particularly in astigmatism and related low-order asymmetric terms. This trend is consistent with modelling predictions and reflects stiffness and thickness variation introduced by fibre steering. The two mirrors exhibit comparable surface roughness (Table 7), with no evidence of high-frequency surface irregularities, indicating good manufacturing quality. The RTS mirror shows a modest increase in roughness at mid-radius, but differences remain small relative to global deformation magnitudes.

To avoid ambiguity in interpretation, it is important to distinguish between the quantities evaluated by modelling and experiment. The finite element analysis quantifies the intrinsic thermoelastic response of an ideal, stress-free laminate under spatially uniform temperature change, governed primarily by laminate-level CTE and global stiffness. In contrast, the thermomechanical experiments measure the response of the as-manufactured mirrors, which include residual stresses from curing, a shifted stress-free temperature, non-uniform heating (≈20 °C in-plane gradient), and gravity/support effects. A fully coupled simulation including these effects was not considered here, as the objective is to isolate intrinsic laminate behaviour under controlled conditions and enable a direct, like-for-like comparison between laminate concepts. Consequently, the experimental observations do not represent a direct validation of intrinsic thermoelastic behaviour, but rather the sensitivity of the as-manufactured surface figure to thermal perturbation under the specific test conditions.

Table 7
Surface roughness of straight-fibre and RTS mirrors (mean ± SD).

Metric	Straight-fibre (Centre)	Straight-fibre (Mid-radius)	RTS (Centre)	RTS (Mid-radius)
R_a(μm)	0.207 ± 0.004	0.308 ± 0.036	0.391 ± 0.010	0.513 ± 0.007
R_q(μm)	0.257 ± 0.004	0.388 ± 0.046	0.490 ± 0.013	0.636 ± 0.010
R_z(μm)	1.316 ± 0.06	2.036 ± 0.22	2.55 ± 0.07	3.286 ± 0.10

Thermomechanical testing shows that surface error decreases at elevated temperature, primarily due to relaxation of cure-induced residual stresses. The straight-fibre mirror exhibits a significant reduction in RMS surface error from ~ 234.9 μm to ~ 152.2 μm (Peak to valley (*PV*): ~577.5 μm to ~ 359.7 μm), indicating substantial stress relaxation. In contrast, the RTS mirror shows a smaller change (RMS: ~111.1 μm to ~ 124.5 μm; *PV*: ~312.2 μm to ~ 299.7 μm), indicating reduced sensitivity of the as-manufactured shape to thermal perturbation under the imposed non-uniform heating conditions. Zernike decomposition ($N \leq 6$) confirms that these variations are dominated by low-order modes, consistent with the global deformation behaviour predicted by the models. Accordingly, the experimental results should be interpreted as demonstrating qualitative agreement in deformation modes and relative sensitivity, rather than quantitative validation of uniform-temperature

thermoelastic predictions. Within this context, the smaller variation observed for the RTS laminate indicates improved stability of the residual-stress-driven shape, while the intrinsic thermoelastic response remains comparable between the two laminates, as predicted by FE analysis. Given the presence of thermal gradients and measurement uncertainty, differences at the level of tens of micrometres should be interpreted with caution, whereas the observed changes in global deformation and consistent trends across repeated measurements are considered reliable.

Differential scanning calorimetry confirmed a high and uniform degree of cure across both mirrors. An uncured IM7/8552 baseline yielded a total reaction enthalpy of ~ 250.5 J/g, used to quantify cure. The straight-fibre laminate showed a residual enthalpy of 16.5 ± 0.4 J/g (~93% cure), while the RTS laminate exhibited 12.2 ± 6.2 J/g (~95% cure) and a glass transition temperature of ~ 226.8 °C. Low residual enthalpy and limited spatial variation (centre, mid-radius, edge) indicate uniform cure in both cases. The slightly lower ΔH_r and higher T_g for RTS suggest a marginally greater effective cure state, potentially linked to local thickness variation and thermal history. Overall, both laminates achieve near-complete and spatially uniform cure, supporting the assumption of homogeneous material properties and indicating that deformation is governed by global residual stresses rather than cure variability. The measured degree of cure and deformation trends are consistent with the assumptions and predictions of the CHILE-based process model, providing experimental support for the adopted modelling framework.

Flexural testing was performed on coupons extracted from the demonstrators using three- and four-point bending (ASTM D7264, n = 5), with representative responses shown in Fig. 14 and properties summarised in Table 8. The straight-fibre laminate exhibits greater flexural modulus and strength, characterised by a steeper initial slope and higher peak stress, whereas the RTS laminate shows reduced stiffness and slightly lower strength, retaining approximately 85–90% of the value. This reduction is attributed to fibre steering and the associated thickness and orientation variations.

The two test configurations exhibit systematically different responses due to their distinct stress states. In three-point bending, failure is dominated by maximum tensile and compressive stresses at the outer fibre layers under a localised loading point, resulting primarily in fibre-dominated failure mechanisms such as tensile fracture and compressive kinking (Fig. 15(a,b)). In contrast, four-point bending introduces a constant bending moment region with reduced stress gradients but increased interlaminar shear (τ_{13}, τ_{23}), promoting earlier interlaminar damage initiation and matrix/interface-controlled failure (Fig. 15(c,d)).

The transition in failure mode directly influences the measured stiffness. The lower apparent modulus observed in four-point bending arises from the increased contribution of interlaminar shear and progressive damage within the constant-moment region, leading to earlier stiffness degradation compared to the more fibre-dominated response in three-point bending. Consequently, three-point bending shows a well-defined linear elastic region, whereas four-point bending exhibits lower apparent modulus, greater deformation prior to failure, and increased scatter due to sensitivity to fixture compliance and distributed damage evolution. Therefore, flexural modulus values from the two methods are not directly comparable and should be interpreted in a relative sense. Despite differences in absolute values, both test methods consistently indicate the same trend (straight-fibre > RTS in stiffness and strength), confirming the reliability of the observed behaviour.

Table 8
Flexural properties of straight-fibre and RTS coupons (mean ± SD).

Test method	Laminate	Flexural modulus (GPa)	Flexural strength (MPa)
Three-point bending	Straight-fibre	76.84 ± 2.66	1031.00 ± 36.7
Three-point bending	RTS	47.98 ± 0.99	917.1 ± 41.1
Four-point bending	Straight-fibre	27.39 ± 2.25	528.0 ± 20.7
Four-point bending	RTS	17.23 ± 1.19	446.7 ± 36.8

Reference testing on unidirectional IM7/8552 laminates produced strengths of ~ 1980 ± 256 MPa (three-point) and ~ 1290 ± 170 MPa (four-point), with interlaminar shear strength of ~ 60.1 ± 6.1 MPa. Compared with these values, both straight-fibre and RTS laminates exhibit substantially lower strengths as expected, reflecting their multidirectional layups and load redistribution. Interlaminar shear testing (short-beam) further confirms matrix/interface-dominated failure (Fig. 15(e,f)), reinforcing that shear-driven mechanisms govern failure when through-thickness stresses are significant. Microscopy revealed typical fibre-dominated failure mechanisms together with interlaminar shear failure, with no evidence of voids, delamination, or process-induced defects. Overall, these results confirm that fibre steering introduces a stiffness reduction without compromising structural integrity, supporting the suitability of RTS laminates for load-bearing precision mirror applications.

5. Conclusions

This study presents a design–manufacture–validation framework that links modelling, optimisation, manufacturing, and experimental validation for straight-fibre and Rapid Tow Shearing (RTS) composite mirror substrates for space-based laser communication systems. A

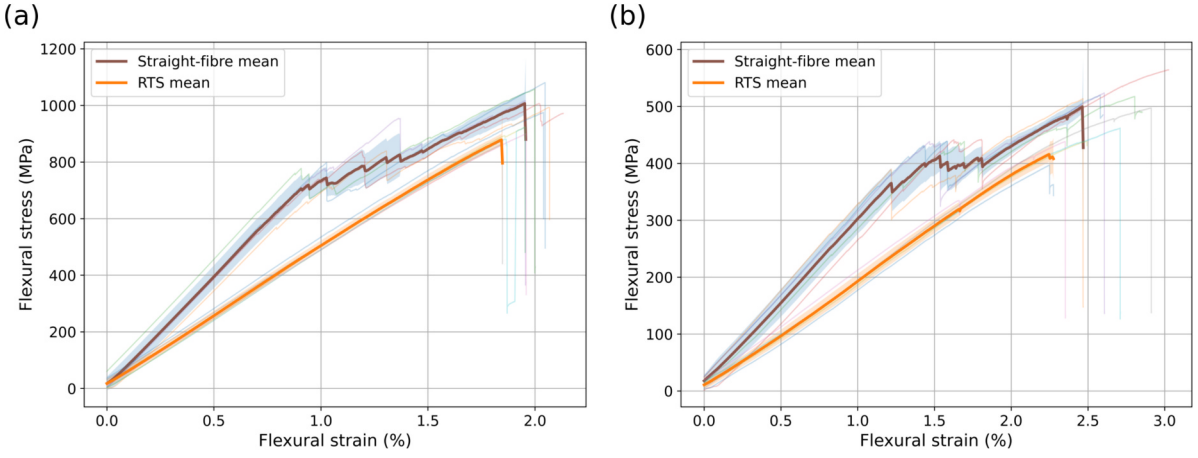


Fig. 14. Flexural stress–strain response: (a) three-point bending; (b) four-point bending (thin lines: specimens; thick line: mean).

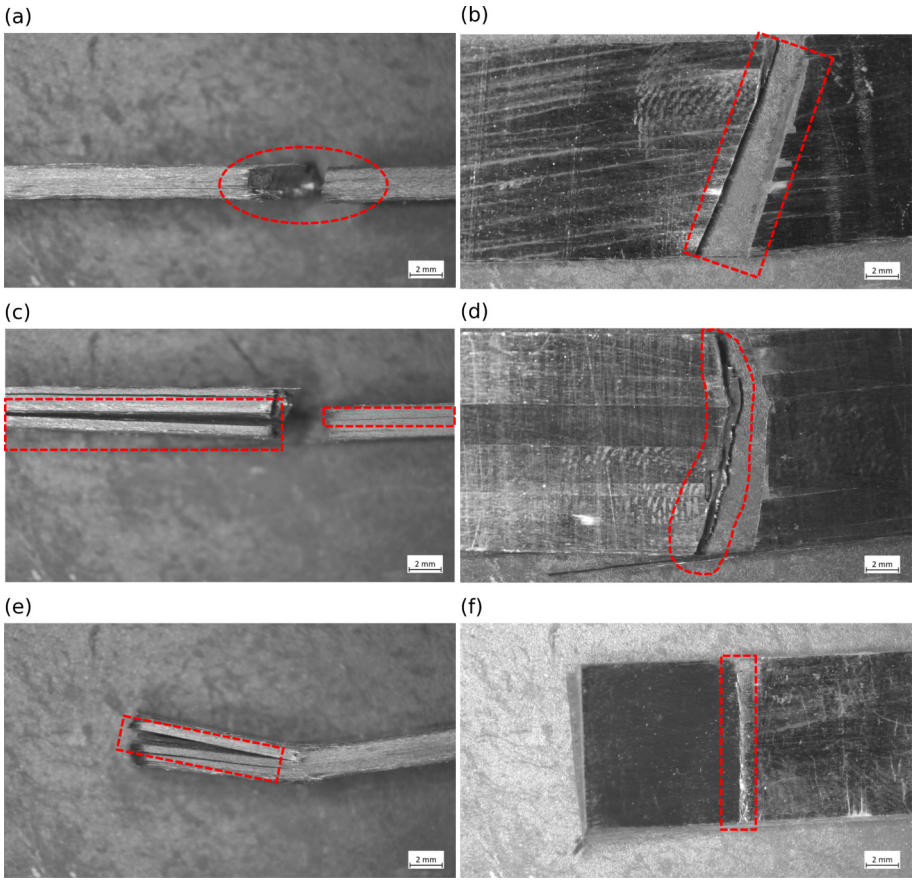


Fig. 15. Microscopy of failure modes in reference coupons: (a, b) three-point bending; (c, d) four-point bending; (e, f) interlaminar shear (short-beam).

consistent, like-for-like comparison was performed under identical geometry, boundary conditions, and load cases, including launch, thermoelastic, hygroscopic, and cure-induced effects. Both laminate concepts satisfy the launch stiffness requirement, with first natural frequencies of approximately 153 Hz for the straight-fibre design and 145 Hz for the RTS design, while exhibiting large in-plane strength margins, indicating that stiffness rather than strength governs the design. RTS enables an approximately 11% reduction in areal density compared with straight-fibre mirrors while maintaining sufficient structural performance, demonstrating its effectiveness for mass-efficient stiffness tailoring. Thermoelastic deformation is identified as the dominant contributor to in-orbit figure change, with both laminates exhibiting similar RMS surface displacement in the range of 62 to 69 μm. This indicates that thermoelastic behaviour is governed primarily by laminate-level properties, particularly effective coefficients of thermal expansion and global bending stiffness, rather than local fibre steering. Hygroscopic distortion is small but non-negligible, while cure-induced deformation is larger in magnitude but dominated by low-order modes and therefore potentially correctable through process or tooling strategies.

Experimental validation confirms high manufacturing quality, uniform cure, and absence of significant defects. Surface metrology and Zernike analysis show that deformation is dominated by low-order global modes, consistent with modelling predictions. RTS introduces increased non-axisymmetric and higher-order residual components but does not generate high-frequency surface errors or compromise structural integrity. Overall, RTS provides additional design freedom for mass reduction without degrading global thermoelastic stability but does not fundamentally alter the governing deformation mechanisms of composite mirrors. Instead, passive stability is primarily limited by the intrinsic thermal behaviour of the material system. The novelty of this work lies in the first experimentally validated, like-for-like comparison that explicitly links variable-stiffness laminate design, manufacturing-induced effects, and optical-scale deformation under consistent conditions. The primary contribution is the establishment of an integrated and traceable framework that combines process modelling, structural analysis, and full-field experimental validation to quantify the mass–stability trade-off in composite mirror design. The resulting impact is the provision of a validated design methodology that improves confidence in predictive modelling and demonstrates the practical viability of RTS for mass-efficient, dimensionally stable space optics, while also indicating that future gains in thermoelastic performance will depend on advances in material systems or hybrid architectures rather than stiffness tailoring alone.

CRediT authorship contribution statement

Nenglong Yang: Writing – original draft, Visualization, Validation, Software, Methodology, Investigation, Formal analysis, Data curation, Conceptualization. **Georgios Stamatopoulos:** Writing – review & editing, Methodology, Investigation, Data curation. **Sampreet Sabarad:** Writing – review & editing, Validation, Investigation, Data curation. **Alex Skordos:** Writing – review & editing, Supervision, Resources, Methodology, Funding acquisition, Conceptualization. **Geoffrey Neale:** Writing – review & editing, Supervision.

Declaration of competing interest

The authors declare that they have no known competing financial interests or personal relationships that could have appeared to influence the work reported in this paper.

Acknowledgements

This work was supported by the UK Space Agency through the National Space Innovation Programme (NSIP), grant number KS1-040, in collaboration with ICOMAT Ltd.

Appendix

.

Appendix A. . Cure-dependent thermochemical and mechanical model

This appendix summarises the cure-kinetics, thermophysical, and cure-dependent mechanical relations used in the CHILE simulations for IM7/8552. All models and parameters were adopted from established literature [36–39,41,49,50], without additional fitting. Degree of cure is denoted by α, temperature by T, and fibre volume fraction by v_f.

A1. Cure kinetics.

Cure evolution follows the Johnston–Hubert autocatalytic–diffusion model [36]:

$$\dot{\alpha} = \frac{K\alpha^m(1-\alpha)^n}{1+e^{C(\alpha-\alpha_{c0}-[\alpha_{cT}*T])}} \tag{A1}$$

where the rate constant (K) follows an Arrhenius-type temperature dependence:

$$K = Ae^{\frac{-\Delta E}{RT}} \tag{A2}$$

The exothermic heat release per unit mass of composite (H) was defined as:

$$H = H_R \cdot (1-v_f)\frac{\rho_r}{\rho} \tag{A3}$$

with composite density (ρ) calculated as:

$$\rho = v_f\rho_f + (1-v_f)\rho_r \tag{A4}$$

The corresponding kinetic parameters are presented in Table A1 [36].

Table A1
Cure kinetics parameters for IM7/8552 [36].

Parameter	Symbol	Value	Unit
Total resin heat of reaction	H_R	540×10^3	J/kg
Pre-exponential factor	A	1.528×10^5	1/s
Activation energy	ΔE	6.65×10^4	J/mol
First exponential constant	m	0.8129	–
Second exponential constant	n	2.736	–
Diffusion constant	C	43.09	–
Diffusion constant	α_{cT}	5.475×10^{-3}	1/K
Diffusion constant	α_{c0}	−1.684	–
Initial degree of cure	α_0	0.05	–
Resin density	ρ_r	1301	kg/m^3
Fibre density	ρ_f	1790	kg/m^3
Fibre volume fraction	v_f	0.577	–

A2. Cure-dependent thermophysical properties.

The temperature- and cure-dependent resin specific heat capacity (C_{p_r}) was modelled as [37,38]:

$$C_{p_r} = C_{p_{rb}} + \frac{C_{p_g} - C_{p_{rb}}}{1+e^{k\left[T-T_g-\Delta T_c\right]}} \tag{A5}$$

where the limit specific heat capacities of the resin in the rubber and glass are:

$$C_{p_i} = (1-\alpha)C_{p_{i0}} + \alpha C_{p_{i\infty}} \ (i = rb, g) \tag{A6}$$

$$C_{p_{ij}} = s_{ij}T + c_{ij} (i = rb, g \text{ and } j = 0, \infty) \tag{A7}$$

The glass transition temperature (T_g) was determined using the DeBenedetto equation [39]:

$$T_g = T_{g0} + \frac{\lambda\alpha\left(T_{g\infty} - T_{g0}\right)}{1-(1-\lambda)\alpha} \tag{A8}$$

IM7 fibre specific heat capacity (C_{pf}) was assumed linear with temperature:

$$C_{pf} = 750 + 2.05T \tag{A9}$$

and the composite specific heat capacity (C_p) was determined through a rule of mixtures:

$C_p = w_f C_{pf} + (1-w_f)C_{pr}, w_f = \frac{\nu_f \rho_f}{\rho}$(A10-A11)

The coefficients for the specific heat capacity and glass transition temperature are summarised in Table A2 [37,38].

Table A2
Specific heat and glass transition parameters for IM7/8552 [37,38].

Parameter	Symbol	Value	Unit
Glass coefficient ($\alpha = 0$)	s_{g0}	3.775	J/(kgK^2)
Glass coefficient ($\alpha = 0$)	c_{g0}	730.0	J/(kgK)
Glass coefficient ($\alpha = 1$)	$s_{g\infty}$	3.40	J/(kgK^2)
Glass coefficient ($\alpha = 1$)	$c_{g\infty}$	830.0	J/(kgK)
Rubber coefficient ($\alpha = 0$)	s_{r0}	3.27	J/(kgK^2)
Rubber coefficient ($\alpha = 0$)	c_{r0}	1088.0	J/(kgK)
Rubber coefficient ($\alpha = 1$)	$s_{r\infty}$	2.0	J/(kgK^2)
Rubber coefficient ($\alpha = 1$)	$c_{r\infty}$	1350.0	J/(kgK)
Transition rate	k	0.278	1/°C
Glass transition ($\alpha = 0$)	T_{g0}	−7	°C
Glass transition ($\alpha = 1$)	$T_{g\infty}$	250	°C
Fitting parameter	λ	0.78	–
Transition offset	ΔT_c	−1.5	°C

A3. Thermal conductivity.

Anisotropic and temperature-dependent heat conduction was represented by polynomial functions for the resin and linear relations for the fibre. The resin thermal conductivity (k_r) was defined as [38]:

$k_r = Ak_r + Bk_r T + Ck_r \alpha$(A12)

while fibre conductivities along the longitudinal (k_{lf}) and transverse (k_{tf}) directions were:

$k_{lf} = Ak_{lf} + Bk_{lf} T, k_{tf} = Ak_{tf} + Bk_{tf} T$(A13-A14)

Composite conductivities followed parallel and series–parallel models [38]:

$k_{11} = \nu_f k_{lf} + (1-\nu_f)k_r$(A15)

$$k_{22} = k_{33} = \nu_f k_r\left(\frac{k_{tf}}{k_r}-1\right) + k_r\left(\frac{1}{2}-\frac{k_{tf}}{2k_r}\right) + k_r\left(\frac{k_{tf}}{k_r}-1\right)\sqrt{\nu_f^2 - \nu_f + \frac{\left(\frac{k_{tf}}{k_r}+1\right)^2}{\left(\frac{2k_{tf}}{k_r}-2\right)^2}} \tag{A16}$$

The corresponding thermal conductivity parameters used in these relations are summarised in Table A3 [38].

Table A3
Thermal conductivity parameters for IM7/8552 [38].

Parameter	Symbol	Value	Unit
Resin base conductivity constant	Ak_r	0.148	W/m/°C
Resin temperature coefficient	Bk_r	3.43×10^{-4}	W/m/°C^2
Resin cure-degree coefficient	Ck_r	6.07×10^{-2}	W/m/°C
Fibre longitudinal base conductivity constant	Ak_{lf}	7.69	W/m/°C
Fibre longitudinal temperature coefficient	Bk_{lf}	1.56×10^{-2}	W/m/°C^2
Fibre transverse base conductivity constant	Ak_{tf}	2.4	W/m/°C
Fibre transverse temperature coefficient	Bk_{tf}	5.07×10^{-4}	W/m/°C^2

A4. Cure-dependent mechanical properties.

The temperature- and cure-dependent modulus of the resin (E_r), was modelled as a function of the reduced temperature (T^*) [36]:

$$E_r = \begin{cases} E_r^0, & T^* < T_{C1}^* \\ E_r^0 + \dfrac{T^* - T_{C1}^*}{T_{C2}^* - T_{C1}^*}\left(E_r^\infty - E_r^0\right), & T_{C1}^* \le T^* \le T_{C2}^* \\ E_r^\infty, & T^* > T_{C2}^* \end{cases} \tag{A17}$$

where:

$T^* = \left(T_g^0 + a_{Tg}{}^* \alpha\right) - T, T_{C1}^* = T_{C1a}$(A18)

The temperature- and cure-dependent Poisson's ratio of the resin (ν_r) and shear modulus (G_r) of the resin were then:

$$\nu_r = \frac{1}{2}\left[1 - \frac{E_r(1-2\nu^{\infty})}{E_r^{\infty}}\right] \text{(A19)}$$

$$G_r = \frac{E_r}{2(1+\nu_r)} \text{(A20)}$$

The corresponding temperature- and cure-dependent constants used in these relations are summarised in Table A4 [36].

Table A4
Temperature- and cure-dependent mechanical properties of Hexcel 8552 epoxy resin [36].

Parameter	Symbol	Value	Unit
Unrelaxed modulus	E_r^{∞}	4.67×10^9	Pa
Relaxed modulus	E_r^0	4.67×10^6	Pa
Lower critical T^*	T_{C1a}	−45.7	K
Upper critical T^*	T_{C2}^*	−12	K
Glass transition ($\alpha = 0$)	T_g^0	268	K
Glass transition variation	a_{Tg}	220	K
Unrelaxed Poisson's ratio	ν^{∞}	0.37	–

Composite stiffness during cure was computed using Chamis' micromechanics model [41], incorporating the cure-dependent resin properties derived above. The elastic moduli and Poisson's ratios were computed as:

$$E_1 = \nu_f E_{lf} + (1-\nu_f)E_r, E_2 = E_3 = \frac{E_r}{1-\sqrt{\nu_f}\left(1-\frac{E_r}{E_{tf}}\right)} \text{(A21-A22)}$$

$$G_{12} = G_{13} = \frac{G_r}{1-\sqrt{\nu_f}\left(1-\frac{G_r}{G_{12f}}\right)}, G_{23} = \frac{G_r}{1-\sqrt{\nu_f}\left(1-\frac{G_r}{G_{23f}}\right)} \text{(A23-A24)}$$

$$\nu_{12} = \nu_{13} = \nu_f\nu_{12f} + (1-\nu_f)\nu_r, \nu_{23} = \frac{E_2}{2G_{23}} - 1 \text{(A25-A26)}$$

Fibre mechanical properties were assumed constant throughout curing and are summarised in Table A5 [36].

Table A5
Fibre properties used in the IM7/8552 curing simulation model [36].

Parameter	Symbol	Value	Unit
Axial Modulus	E_{lf}	276,000	MPa
Transverse Modulus	E_{tf}	19,500	MPa
In-plane Poisson's ratio	$\nu_{12f} = \nu_{13f}$	0.28	–
Out-of-plane Poisson's ratio	ν_{23f}	0.25	–
In-plane Shear Modulus	$G_{12f} = G_{13f}$	70,000	MPa
Out-of-plane Shear Modulus	G_{23f}	7800	MPa

A5. Cure-dependent CTE.

The temperature- and cure-dependent modulus of the resin CTE (α_r) with reduced temperature (T^*) was expressed as:

$$\alpha_r = \begin{cases} \alpha_r^0, & T^* < T_{C1}^* \\ \alpha_r^0 + \dfrac{T^* - T_{C1}^*}{T_{C2}^* - T_{C1}^*}\left(\alpha_r^{\infty} - \alpha_r^0\right), & T_{C1}^* \le T^* \le T_{C2}^* \\ \alpha_r^{\infty}, & T^* > T_{C2}^* \end{cases} \text{(A27)}$$

with reduced temperature defined by Eq. (A18). Composite CTEs during cure were computed using Chamis' micromechanics model [41]:

$$\alpha_{11} = \frac{\alpha_{f1}E_{lf}\nu_f + \alpha_r E_r(1-\nu_f)}{E_{lf}\nu_f + E_r(1-\nu_f)} \text{(A28)}$$

$$\alpha_{22} = \alpha_{33} = \alpha_{f2}\sqrt{\nu_f} + (1-\sqrt{\nu_f})\left(1 + \nu_f\nu_r\frac{E_{lf}}{E_{lf}\nu_f + E_r(1-\nu_f)}\right)\alpha_r \text{(A29)}$$

The relevant fibre and resin CTE values are presented in Table A6.

Table A6
Thermal expansion parameters for IM7 fibre and Hexcel 8552 epoxy resin [49,50].

Parameter	Symbol	Value	Unit
Unrelaxed resin CTE	α_r^{∞}	5.66×10^{-5}	K^{-1}
Relaxed resin CTE	α_r^0	2.86×10^{-5}	K^{-1}
Fibre axial CTE	α_{f1}	-0.54×10^{-6}	K^{-1}
Fibre transverse CTE	α_{f2}/α_{f3}	10.08×10^{-6}	K^{-1}

A6. Cure shrinkage model.

Chemical shrinkage during curing was modelled by applying incremental shrinkage strains throughout the process. The total composite shrinkage strain in the principal material directions was defined as:

$$\varepsilon_{ij}^{S} = C_{ij}^{S}\cdot\left(\varepsilon_{ij}^{s(k)} - \varepsilon_{ij}^{s(k-1)}\right) \text{(A30)}$$

where the resin shrinkage strain is:

$$\varepsilon_{r}^{s} = \left(1 + V_{r}^{s}\right)^{1/3} - 1 \text{(A31)}$$

The composite shrinkage coefficients were expressed as:

$$C_{11}^{S} = \frac{\left(1-\nu_f\right)E_r}{\left(1-\nu_f\right)E_r + \nu_f E_{lf}} \text{(A32)}$$

$$C_{22}^{S} = C_{33}^{S} = \left(\nu_r + 1\right)\left(1 - \nu_f\right) - \nu_{12}C_{11}^{S} \text{(A33)}$$

The volumetric cure shrinkage (V_r^S) evolves with the degree of cure according to [36]:

$$V_{r}^{S} = \begin{cases} 0, & \alpha < \alpha_{C1} \\ A\alpha_S + \left(V_r^{S\infty} - A\right)\alpha_S^2, & \alpha_{C1} \le \alpha < \alpha_{C2} \\ V_r^{S\infty}, & \alpha \ge \alpha_{C2} \end{cases} \text{(A34)}$$

$$\alpha_S = \frac{\alpha - \alpha_{C1}}{\alpha_{C2} - \alpha_{C1}} \text{(A35)}$$

The material parameters for the cure shrinkage model are summarised in Table A7.

Table A7
Cure shrinkage parameters for IM7/8552 [36].

Parameter	Symbol	Value
Onset of shrinkage	α_{C1}	0.055
End of shrinkage	α_{C2}	0.651
Total volumetric resin shrinkage	$V_r^{S\infty}$	0.099
Nonlinearity coefficient	A	0.173

Data availability

Data underlying this study can be accessed through the Cranfield University repository at https://doi.org/10.57996/cran.ceres-2842.

References

[1] T. Ștefanov, H.V.R. Maraka, P. Meagher, J. Rice, W. Sillekens, D.J. Browne, Thin film metallic glass broad-spectrum mirror coatings for space telescope applications, Journal of Non-Crystalline Solids: X 7 (2020) 100050.

[2] I. Trumper, P. Hallibert, J.W. Arenberg, H. Kunieda, O. Guyon, H.P. Stahl, D. W. Kim, Optics technology for large-aperture space telescopes: from fabrication to final acceptance tests, Adv. Opt. Photon. 10 (3) (2018) 644–702.

[3] B.C. Kim, P.M. Weaver, K. Potter, Manufacturing characteristics of the continuous tow shearing method for manufacturing of variable angle tow composites, Compos. A Appl. Sci. Manuf. 61 (2014) 141–151.

[4] G. Rousseau, R. Wehbe, J. Halbritter, R. Harik, Automated Fiber Placement Path Planning: a state-of-the-art review, Computer-Aided Design & Applications 16 (2) (2019) 172–203.

[5] S. Carosella, S. Hügle, F. Helber, P. Middendorf, A short review on recent advances in automated fiber placement and filament winding technologies, Compos. B Eng. 287 (2024) 111843.

[6] B.C. Kim, K. Potter, P.M. Weaver, Continuous tow shearing for manufacturing variable angle tow composites, Compos. A Appl. Sci. Manuf. 43 (8) (2012) 1347–1356.

[7] L. Parnas, S. Oral, Ü. Ceyhan, Optimum design of composite structures with curved fiber courses, Compos. Sci. Technol. 63 (7) (2003) 1071–1082.

[8] D.H.J.A. Lukaszewicz, C. Ward, K.D. Potter, The engineering aspects of automated prepreg layup: history, present and future, Compos. B Eng. 43 (3) (2012) 997–1009.

[9] X. Legrand, D. Kelly, A. Crosky, D. Crépin, Optimisation of fibre steering in composite laminates using a genetic algorithm, Compos. Struct. 75 (1) (2006) 524–531.

[10] S. Setoodeh, M.M. Abdalla, Z. Gürdal, Design of variable–stiffness laminates using lamination parameters, Compos. B Eng. 37 (4) (2006) 301–309.

[11] A.W. Blom, S. Setoodeh, J.M.A.M. Hol, Z. Gürdal, Design of variable-stiffness conical shells for maximum fundamental eigenfrequency, Comput. Struct. 86 (9) (2008) 870–878.

[12] M.W. Hyer, H.H. Lee, The use of curvilinear fiber format to improve buckling resistance of composite plates with central circular holes, Compos. Struct. 18 (3) (1991) 239–261.

[13] M.R. Wisnom, M. Gigliotti, N. Ersoy, M. Campbell, K.D. Potter, Mechanisms generating residual stresses and distortion during manufacture of polymer–matrix composite structures, Compos. A Appl. Sci. Manuf. 37 (4) (2006) 522–529.

[14] M. Postman, T. Brown, K. Sembach, J. Tumlinson, C.M. Mountain, R. Soummer, M. Giavalisco, D. Calzetti, W. Traub, K. Stapelfeldt, W. Oegerle, T. Hyde, R. Rich, H.P. Stahl, Advanced Technology Large-Aperture Space Telescope: science drivers and technology developments, Opt. Eng. 51 (1) (2012) 011007.

[15] C. Sandin, L. Allen, E. Amatucci, J. Arenberg, R. Carter, J. Corsetti, M. DiPirro, M. East, L. Fantano, A. Flores, J.S. Knight, D. Leisawitz, P. Lightsey, G. Martins, T. Mooney, A. Nordt, J. Steeves, Materials evaluation for the Origins Space Telescope, J. Astron. Telesc. Instrum. Syst. 7 (1) (2021) 011011.

[16] R. Romeo, R. Martin, S. Restaino, C. Wilcox, J. Andrews, T. Martinez, F. Santiago, J. Clark, J. Walton, S. Tearez, Ultra-lightweight, Deployable 1m-Class Optical Telescope for SSA applications. 2007 AMOS Conference Proceedings(advanced Maui Optical and Optical and Space Surveillance Technologies Conference), 2007.

[17] R. Romeo, R. Martin, M. Molina, G. Sardo, G. Laurenti, Replicated carbon fiber RICH mirror for AMS-02, Space Telescopes and Instrumentation II: Ultraviolet to Gamma Ray, SPIE, Orlando, Florida, United States, 2006, p. 62663J.

[18] H. Kaushal, G. Kaddoum, Optical Communication in Space: challenges and Mitigation Techniques, IEEE Communications Surveys & Tutorials 19 (1) (2017) 57–96.

[19] R.Y. Kim, A.S. Crasto, G.A. Schoeppner, Dimensional stability of composite in a space thermal environment, Compos. Sci. Technol. 60 (12) (2000) 2601–2608.

[20] E. Toto, L. Lambertini, S. Laurenzi, M.G. Santonicola, Recent advances and challenges in Polymer-based Materials for Space Radiation Shielding, Polymers 16 (3) (2024) 382.

[21] D. González-Bárcena, J. Bermejo-Ballesteros, I. Pérez-Grande, Á. Sanz-Andrés, Selection of time-dependent worst-case thermal environmental conditions for Low Earth Orbit spacecrafts, Adv. Space Res. 70 (7) (2022) 1847–1868.

[22] O.G. Kravchenko, S.G. Kravchenko, R.B. Pipes, Chemical and thermal shrinkage in thermosetting prepreg, Compos. A Appl. Sci. Manuf. 80 (2016) 72–81.

[23] E.V. Morozov, A.V. Lopatin, Design, analysis, manufacture and testing of the spacecraft mirror antenna with the composite high precision and size-stable solid surface reflector, Compos. Struct. 301 (2022) 116185.

[24] V. Villalba Corbacho, H. Kuiper, E. Gill, Review on thermal and mechanical challenges in the development of deployable space optics, J. Astron. Telesc. Instrum. Syst. 6 (1) (2020) 010902.

[25] R.K. Banyal, B. Ravindra, S. Chatterjee, Opto-thermal analysis of a lightweighted mirror for solar telescope, Opt. Express 21 (6) (2013) 7065–7081.

[26] J.D. Johnston, J.M. Howard, G.E. Mosier, K.A. Parrish, M.A. McGinnis, A.M. Bluth, K. Kim, K.Q. Ha, Integrated modeling activities for the James Webb Space Telescope: structural-thermal-optical analysis, Optical, Infrared, and Millimeter Space Telescopes, SPIE, Glasgow, United Kingdom, 2004, p. 5487.

[27] M. Smith, ABAQUS/Standard User's Manual, Dassault Systèmes Simulia Corp (2009).

[28] H. Corporation, HexPly® 8552 EU Data Sheet, 2023.

[29] K. Marlett, Y. Ng, J. Tomblin, Hexcel 8552 IM7 unidirectional prepreg 190 gsm & 35% RC qualification material property data report, NCAMP (2011).

[30] P.P. Camanho, P. Maimí, C.G. Dávila, Prediction of size effects in notched laminates using continuum damage mechanics, Compos. Sci. Technol. 67 (13) (2007) 2715–2727.
[31] J.W. Miles, On Structural Fatigue under Random Loading, Journal of the Aeronautical Sciences 21 (11) (1954) 753–762.
[32] A. Revathi, M.S. Murugan, S. Srihari, N. Jagannathan, C. Manjunatha, Effect of hot-wet conditioning on the mechanical and thermal properties of IM7/8552 carbon fiber composite, Indian Journal of advances in Chemical, Science 2 (2014) 84–88.
[33] M.S. Corporation, Marc 2023.2 User Documentation, Volume A: Theory and User Information, (2023).
[34] A. Engineering, AniForm Suite User Manual, AniForm Engineering B.v. (2023).
[35] A. Johnston, R. Vaziri, A. Poursartip, A Plane Strain Model for Process-Induced Deformation of Laminated Composite Structures, J. Compos. Mater. 35 (16) (2001) 1435–1469.
[36] A.A. Johnston, An integrated model of the development of process-induced deformation in autoclave processing of composite structures., The University of British Columbia, 1997.
[37] D. Van Ee, A. Poursartip, HexPly 8552 Material Properties Database for use with COMPRO CCA and RAVEN, Version 0.9. NCAMP. Wichita, KS (2009).
[38] J.-P.-H. Belnoue, T. Mesogitis, O.J. Nixon-Pearson, J. Kratz, D.S. Ivanov, I. K. Partridge, K.D. Potter, S.R. Hallett, Additional data for "Understanding and predicting defect formation in automated fibre placement pre-preg laminates", published in Composites Part a: Applied Science and Manufacturing, Tech. Rep. 6 (2017).
[39] A.T. DiBenedetto, Prediction of the glass transition temperature of polymers: a model based on the principle of corresponding states, J Polym Sci B 25 (9) (1987) 1949–1969.
[40] A.B. Hexagon, Marc 2023.2 Volume B: Element Library, Hexagon Manufacturing Intelligence, Irvine, CA, USA, 2023.
[41] C.C. Chamis, Simplified composite micromechanics equations for hygral, thermal and mechanical properties, SAMPE Quarterly, Ann. Conf. of the Society of the Plastics Industry (SPI), Reinforced Plastics/composites Inst. (1984) 14–23.
[42] G. Fives, Quality inspection services for precision-machined components, 2025. https://www.fivesgroup.com/high-precision-machines/grinding-ultra-precision/engineering-partnership/quality-inspection-services.
[43] T-Mac, T-Mac Laser Tracker Systems Brochure, (2009).
[44] V.N. Mahajan, Zernike annular polynomials for imaging systems with annular pupils, J. Opt. Soc. Am. 71 (1) (1981) 75–85.
[45] L. Taylor Hobson, Form Talysurf 120L Surface Profilometer: Product Specification and User Guide, (2015).
[46] International Organization for Standardization, Geometrical Product Specifications (GPS) — Surface texture: Profile method — Terms, definitions and surface texture parameters, ISO 4287:1997, International Organization for Standardization, Geneva, Switzerland, 1997.
[47] A.B. Hexagon, Absolute Scanner AS1 Data Sheet, Hexagon Manufacturing, Intelligence (2021).
[48] International Organization for Standardization, Fibre-reinforced plastic composites — Determination of apparent interlaminar shear strength by short-beam method, ISO 14130:1997, International Organization for Standardization, Geneva, Switzerland, 1997.
[49] S.P. Shah, M. Maiarù, Effect of Manufacturing on the Transverse Response of Polymer Matrix Composites, Polymers 13 (15) (2021) 2491.
[50] M.H. Nguyen, R.J. D'Mello, A.M. Waas, Use of a neural network constitutive model for the size-dependent effects of curing on the deformation response and failure of fiber-reinforced polymer matrix composites, Arch. Appl. Mech. 93 (1) (2023) 369–387.



https://dspace.org/

Thermoelastic optimisation of fibre-steered composite mirrors for space-based laser communication systems

Yang, Nenglong; Stamatopoulos, Georgios; Sabarad, Sampreet; Skordos, Alexandros A.; Neale, Geoffrey

2026-08
Elsevier
https://doi.org/10.1016/j.matdes.2026.116430
Yang N, Stamatopoulos G, Sabarad S, et al., (2026) Thermoelastic optimisation of fibre-steered composite mirrors for space-based laser communication systems. Materials & Design, Volume 268, August 2026, Article number 116430

Downloaded from a DSpace repository. https://dspace.org/